ADVANCING EARTH AND SPACE SCIENCE

JGR Solid Earth

RESEARCH ARTICLE
10.1029/2019JB017508

Key Points:
- CSC and Mohr-Coulomb fault slip tendency analyses are used to investigate multifault earthquakes
- The fault system responsible for the 2010 M_w7.1 Darfield earthquake is probabilistically favored to rupture in multifault earthquakes
- Fault network geometries and slip tendencies influence earthquake frequency-magnitude distributions and maximum magnitude estimations

Correspondence to:
M. C. Quigley,
mark.quigley@unimelb.edu.au

Citation:
Quigley, M. C., Jiménez, A., Duffy, B., & King, T. R. (2019). Physical and statistical behavior of multifault earthquakes: Darfield earthquake case study, New Zealand. *Journal of Geophysical Research: Solid Earth*, *124*. https://doi.org/10.1029/2019JB017508

Received 5 FEB 2019
Accepted 12 APR 2019
Accepted article online 15 APR 2019

Physical and Statistical Behavior of Multifault Earthquakes: Darfield Earthquake Case Study, New Zealand

M. C. Quigley[1], A. Jiménez[2], B. Duffy[1], and T. R. King[1]

[1]School of Earth Sciences, The University of Melbourne, Melbourne, Victoria, Australia, [2]Departmento de Ciencias de la Computación e Inteligencia Artificial, Universidad de Granada, Granada, Spain

Abstract We use Coulomb stress change (CSC) analyses and seismicity data to model the physical and statistical behavior of the multifault source of the 4 September 2010 M_w 7.1 Darfield earthquake in New Zealand. Geodetic and seismologic data indicate this earthquake initiated on a severely misoriented reverse fault and propagated across a structurally complex fault network including optimally oriented faults. The observed rupture sequence is most successfully modeled if maximum CSC imposed by rupture of the hypocentral fault on to receiver faults exceeds theoretical threshold values of 1 to 5 MPa that are assigned based on fault slip tendency and stress drop analyses. CSC modeling using the same criteria but initiating the earthquake on other faults in the network results in a multifault rupture cascade for five of seven scenarios. Analysis of earthquake frequency-magnitude distributions indicates that a Gutenberg-Richter frequency-magnitude distribution for the near-source region cannot be rejected in favor of a characteristic earthquake distribution. However, characteristic behavior is more favored probabilistically because ruptures initiating on individual source faults in the system are statistically more likely to cascade into multifault ruptures with larger amalgamated M_w ($M_w^{max} = 7.1$) than to remain confined to the hypocentral source fault ($M_w = 6.3$ to 6.8). Our favored hypothesis is that system rupture behavior is regulated by misoriented faults that occupy critical geometric positions within the network, as previously proposed for the 2010 El Mayor-Cucapah earthquake in Baja California. Other fault networks globally may exhibit similar physical and statistical behaviors.

1. Introduction

Many continental earthquakes result from the rupture of multiple faults with different geometries, rupture kinematics, and seismic moments (M_o; Beavan et al., 2012; Eberhart-Phillips et al., 2003; Fletcher et al., 2016a, 2016b; Hamling et al., 2017). Understanding how fault networks rupture is important because the coseismic amalgamation of multifault ruptures increases the M_o of the earthquake relative to the M_o sourced from individual fault or fault segment ruptures (Elliott et al., 2012; Fletcher et al., 2016a, 2016b). This has implications for estimating regional seismic hazard parameters such as the maximum moment magnitude (M_w^{max}; Kijko, 2004) and for characterizing earthquake frequency-magnitude distributions (Parsons et al., 2012). In regions of distributed continental faulting, seismogenic crustal thickness limits fault segment lengths to approximately 10 to 30 km and M_w^{max} potentials to 6–7 (Klinger, 2010; Litchfield et al., 2014; Pacheco et al., 1992; Scholz, 1997; Stock & Smith, 2000; Triep & Sykes, 1997). Fault size (Rundle, 1989) and earthquake frequency-magnitude distributions (Gutenberg & Richter, 1944; Ishimoto & Lida, 1939) generally adhere to Gutenberg-Richter (G-R) power law scaling with mean b values ≈ 1 (Spada et al., 2013). However, if fault network geometries fundamentally control rupture behavior (Angelier, 1989; Nieto-Obregón, 1989), such as by regulating network stability and rupture of misoriented "keystone" faults (Fletcher et al., 2016b), then self-organized fault systems may be sustained at supercritical stress (Scholz, 2010) until cascading avalanche-type earthquake sequences occur (Bak et al., 1988; Olami et al., 1992).

Rupture cascades might occur as a single multifault earthquake with continuous M_o release (Elliott et al., 2012; Hamling et al., 2017) or in spatiotemporally "clustered" series of earthquakes separated by seconds to years on proximal faults with expected recurrence intervals of $>10^3$–10^5 years (Beavan et al., 2012; Bowman, 1992; Walters et al., 2018). Theoretically, these types of behaviors might induce significant deviations from G-R scaling. For example, because the M_w of a multifault earthquake amalgamates smaller M_w earthquakes sourced from individual faults into a single event, the population of moderate M_w single-fault earthquakes in this spatial-temporal domain may be lower than predicted from G-R (Parsons et al., 2012). Depending on the recurrence rate, larger M_w earthquakes may occur less or more frequently than suggested from extrapolation of G-R scaling of smaller M_w earthquakes (i.e., characteristic earthquake model; Schwartz & Coppersmith, 1984; Wesnousky, 1994), although large statistical and geological uncertainties exist in distinguishing G-R from characteristic earthquake behaviors (Howell, 1985; Kagan, 1993, 1996; Kagan et al., 2012; Naylor et al., 2009; Page et al., 2011; Page & Felzer, 2015).

Coulomb stress change (CSC) analysis (Cocco & Rice, 2002; Hainzl et al., 2009; Harris, 1998; King et al., 1994; Steacy et al., 2005; Stein et al., 1992) has been used to investigate many multifault earthquake sequences, including multifault rupture cascades (Fletcher et al., 2016a) and spatiotemporally clustered earthquakes (Walters et al., 2018). A major limitation of many CSC studies is the ambiguity with which estimated changes on receiver faults are considered to have been high enough to trigger rupture (Stramondo et al., 2011). A CSC of 0.01 MPa is commonly inferred to represent a minimum value for potential earthquake triggering (Freed, 2005; Harris, 1998, 2000; King et al., 1994; Stein, 1999). However, the CSC threshold to trigger spontaneous rupture on receiver faults concurrent with the hypocentral source fault rupture may be significantly higher. For example, CSC changes of >0.1 MPa (Zhan et al., 2011) on faults proximal to Christchurch, New Zealand, induced by the 2010 Darfield earthquake were insufficient to generate spontaneous rupture; instead, $M_w \geq 6$ earthquakes occurred on these faults several months after the Darfield earthquake. CSC increases of >1 to 1.5 MPa accumulated progressively over days-to-months were required to initiate $M_w > 6$ fault ruptures in the 2016 Central Italy seismic sequence (Walters et al., 2018). Another limitation of CSC analysis is that finite-fault source models have large uncertainties (e.g., source and receiver fault geometry, slip vector orientations, magnitudes, and distributions) resulting from input data uncertainties (e.g., statistical and epistemic uncertainties in seismic and geodetic data), model assumptions (e.g., crustal properties, frictional coefficients), and the model estimation procedure (e.g., nonlinear optimization estimations of geodetic data; Woessner et al., 2012).

Recently, Fletcher et al. (2016b) inverted surface rupture and aftershock data for stress orientations and used Mohr-Coulomb fault slip tendency and CSC analyses to investigate rupture propagation across a complex fault network in the 2010 M_w 7.2 El Mayor-Cucapah in Baja California. Parsons et al. (2012) used CSC analysis to forecast and rank the most likely rupture propagation pathways and earthquake magnitudes for hypothetical rupture scenarios on active faults in California. In this paper, we combine aspects of these approaches and incorporate fault-specific CSC thresholds (CSC_x^{crit}) estimated from seismologic and structural data to investigate the mechanical and statistical behavior of the source faults that ruptured in the 4 September 2010 M_w 7.1 Darfield earthquake in the South Island of New Zealand (Figure 1a).

Our study is motivated by three primary objectives. First, we aim to understand whether the observed multifault rupture observed in the Darfield earthquake is consistent with modeled static stress changes imposed by the hypocentral fault on to receiver faults exceeding a critical rupture initiation threshold (CSC_x^{crit}; where the subscript "x" represents maximum, average, or total stress). We explore the possibility that different values of CSC^{crit} are required to facilitate rupture on different receiver faults because of their diverse geometries and slip tendencies. We acknowledge that other effects (e.g., dynamic stress changes) may be important, but do not analyze these in this study.

Second, we aim to understand whether the observed multifault rupture sequence in the Darfield earthquake is representative of the long-term behavior of this fault system (encompassing $>10^2$ s of predecessor ruptures on the Darfield fault system, as indicated from geophysically identified cumulative offsets across faults in this system; Lawton et al., 2011), or whether the observed sequence was anomalous relative to past rupture behaviors. Since the Darfield earthquake was sourced primarily from the rupture of blind faults (Beavan et al., 2012) paleoseismic studies including derivation of rupture chronologies are limited to the Greendale fault (GF; Hornblow et al., 2014; Figure 1b) and the multifault versus individual fault rupture hypotheses cannot be directly tested through field investigations. Instead, we use the rupture criteria established in our CSC modeling to investigate stress effects if initial rupture occurs on any other fault in the network. This allows us to evaluate which rupture initiation scenarios favor multifault rupture cascades versus single fault ruptures.

Finally, we consider these results in a statistical sense to better understand fault network behavior on earthquake frequency-magnitude distributions and M_w^{max}. Resolving these questions is important for

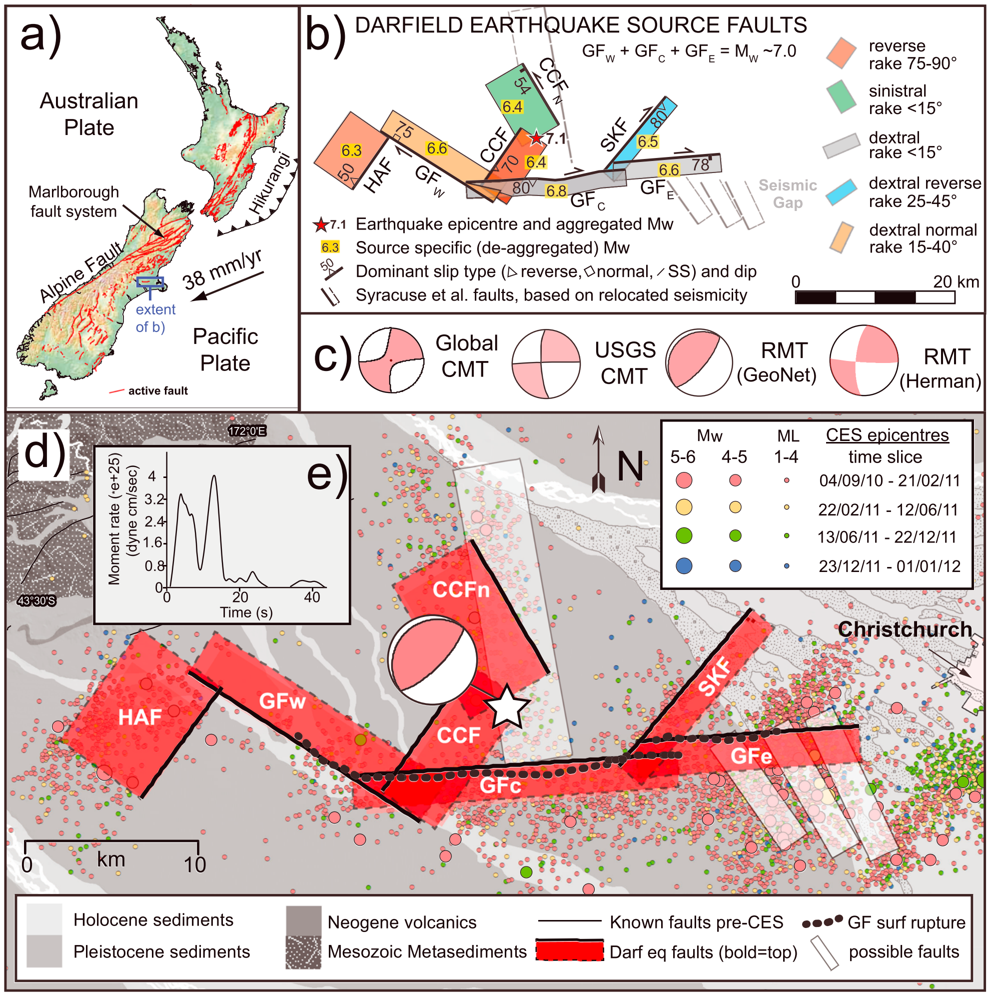

Figure 1. (a) Location of the Darfield earthquake and associated Canterbury earthquake sequence in New Zealand's South Island. Major plate boundary faults (Alpine Fault and Marlborough Faults) traverse the South Island north and west of the study area. Location of active faults (red) from the active fault database (http://data.gns.cri.nz/af/). (b) Fault geometry, slip sense, and M_w contributions for the 4 September 2010 Darfield earthquake based on Beavan et al. (2012). Dips of key faults shown on fault traces. (c) Global centroid moment tensor (CMT) and regional moment tensor (RMT) solutions, showing that the dominant moment release was associated with a strike-slip mechanism, but that the Darfield earthquake initiated on a high-angle reverse fault, as revealed by the Geonet RMT. (d) Aftershock locations and timing relative to the Darfield earthquake source fault network. Red-shaded faults follow Beavan et al. (2012). White shaded possible-faults follow Syracuse et al. (2013). HAF = Hororata Anticline Fault; GF_W = Greendale Fault West; CCF = Charing Cross Fault; CCF_N = Charing Cross Fault North (distinct from Kirwee Fault proposed by Syracuse et al. and shown in white); GF_C = Greendale Fault Central; SKF = Sandy Knolls Fault; GF_E = Greendale Fault East. Location of surface rupture trace from Quigley et al. (2012). (e) Seismic moment release rate plotted versus time after hypocenter rupture from Hayes (2010); the possible origin of distinct moment pulses is discussed in the text.

understanding the rupture behavior and seismic hazard posed by analogous fault systems in New Zealand (Litchfield et al., 2014) and elsewhere (Field et al., 2014).

2. Darfield Earthquake

2.1. Rupture Dynamics and Slip

P wave first motion and regional moment tensor solutions (Gledhill et al., 2010; Figure 1c), and combined interferometric synthetic aperture radar (InSAR) and best fit geodetic models (Beavan et al., 2012), indicate that the 4 September 2010 M_w 7.1 Darfield earthquake initiated on the steeply SE dipping (≈70–80°), NE striking Charing Cross reverse fault (CCF; Figures 1b and 1d). The auxiliary moment tensor solution fault plane is excluded based on InSAR and geodetic data, which indicates E-side-up surface displacement across a steeply southeast dipping reverse fault. Elliott et al. (2012) proposed a dip of ≈60° for the CCF using InSAR and teleseismic data. Other finite fault source models (Atzori et al., 2012; Stramondo et al., 2011) are generally consistent with the Beavan et al. (2012) model and include the CCF with dip estimates of 60–75°. In this study, we use Beavan's finite fault model because it is the only one that utilizes high-precision local geodetic data, aftershock data, and regional moment tensor data (Bannister & Gledhill, 2012) in addition to InSAR. We acknowledge this choice presents an untested source of epistemic uncertainty in our study. A multitude of other small faults defined by aftershock lineaments (Herman et al., 2014; Li et al., 2014; Syracuse et al., 2013; Figures 1b and 1d) have been proposed; however, these other faults are not required to balance the source model-derived moment with the seismologic moment nor improve fits to the surface deformation revealed from InSAR and geodetic data. It is not clear whether they represent continuous, potential planes with the capacity for larger M_w ruptures or structurally discontinuous arrays of smaller faults. As a result, we do not evaluate them further in this study, although they remain a focus of ongoing research (e.g., Lawton et al., 2011).

Holden et al. (2011) present the only published dynamic rupture model (as of October 2018) of the Darfield earthquake. According to their model, the reverse CCF ruptured first, then propagated from the hypocenter in a SW direction toward to the intersection with the GF (Holden et al., 2011) and NW on the strike-slip Charing Cross north fault (CCF_N; Figure 1d). From the CCF-GF junction, the rupture propagated eastward onto the central section of the strike-slip Greendale fault (GF_C), toward the oblique-reverse Sandy Knolls blind fault (SKF) and strike-slip Greendale fault east (GF_E), and westward on to the, oblique-normal Greendale fault west (GF_W), toward the blind thrust Hororata Anticline Fault (HAF). The hypocentral and neighboring faults ruptured dominantly unilaterally, which is consistent with the tendency toward unilateral rupture propagation observed in global large earthquake compilations (McGuire et al., 2002). The interpretation of unilateral rupture propagation is corroborated by increased aftershock activity at the northern and eastern extents of the CCF_N and GF_E fault ruptures respectively (Figure 2); increased stress focusing in the rupture propagation direction is commonly expressed as aftershock clouds surrounding the down-rupture termini of these faults (Gomberg et al., 2003). Geodetic data (Beavan et al., 2012) and inversion modeling of strong-motion data (Holden et al., 2011) suggest that slip on the Hororata anticline blind thrust fault (HAF; Figure 1d) occurred late in the rupture sequence. We do not know whether HAF rupture occurred simultaneously with arrival of the propagating rupture front (Holden et al., 2011) or whether there was a time delay (i.e., 5–7 s) before HAF rupture, as potentially indicated by a temporal gap in the teleseismic moment rate function (Figure 1e; Hayes, 2010).

The GF segments (GF_W, GF_E, and GF_C) contributed the largest M_o release (equivalent to a M_w 6.9–7.0 earthquake, or 6.6 + 6.6 + 6.8 earthquakes) from primarily right-lateral (with some normal slip on the GF_W) ruptures (Figures 1b and 1d). The combined GF_W, GF_E, and CF_C ruptures generated a 29.5 ± 0.5-km-long surface rupture with average and maximum displacements of 2.5 ± 0.1 m and 5.3 ± 0.5 m, respectively (Quigley et al., 2012). Average and maximum displacements in the finite fault models of Beavan et al. (2012) are as follows: GF_W (avg = 1.8 m, max = 4.6 m), GF_E (1.9, 5.6), GF_C (2.8, 7.6), CCF (1.2, 5.6), CCF_N (1.3, 2.5), HAF (1.1, 4.0), and SKF (1.4, 3.3).

M_w contributions from other faults that ruptured during the Darfield earthquake range from 6.3 to 6.5 (Figure 1b). Gledhill et al. (2010) estimate a hypocentral depth of 10.8 km, below an epicenter located approximately 6 km north of the GF surface rupture trace (i.e., coincident with the CCF; Figures 1c and 1d). Strike-slip global and U.S. Geological Survey centroid moment tensors are consistent with the large moment release from the GF (Figure 1c). Pulses in the seismic moment release rate (Figure 1e) add further evidence for complexity in the rupture process (e.g., Hayes et al., 2010); late-stage moment release rate pulses centered on approximately 25 and 40 s could possibly relate to the delayed rupture of the HAF and/or other subsidiary faults (e.g., SKF) peripheral to the CCF and GF segments.

2.2. Magnitude-Frequency Distributions for Darfield Seismic Catalogues

Several studies have analyzed the magnitude-frequency distribution of the 2010–2011 Canterbury earthquake sequence (CES; e.g., Quigley & Forte, 2017; Quigley et al., 2016; Shcherbakov et al., 2012). Most recently, Stirling and Zúñiga (2017) used seismic data (GeoNet earthquake catalogue; September 2010 to

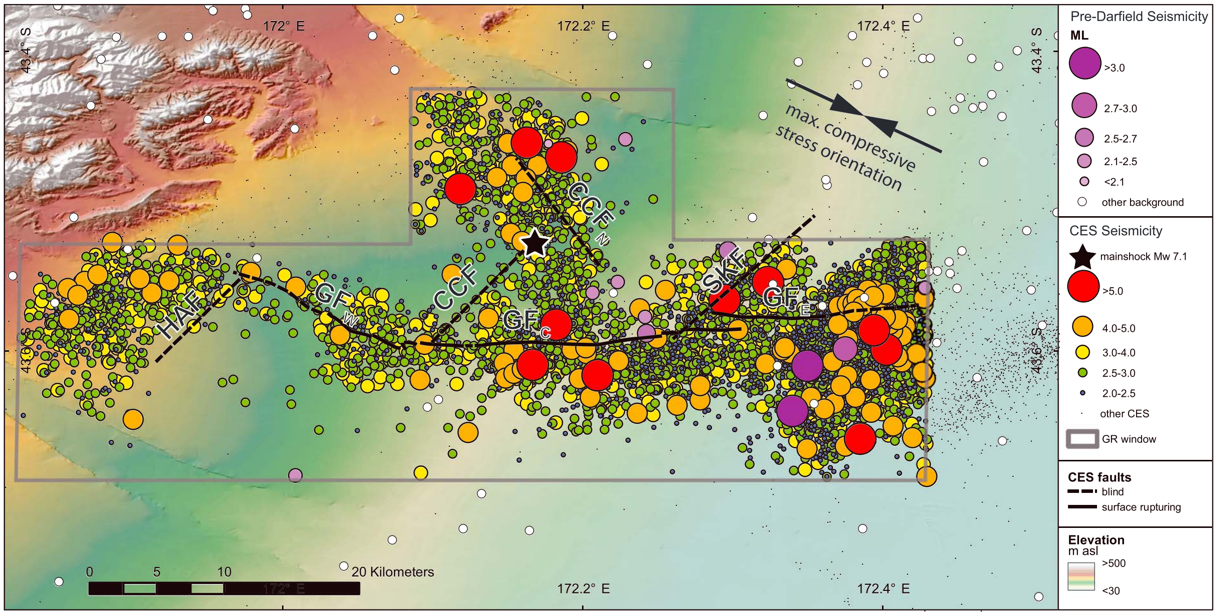

Figure 2. Earthquake epicenters and magnitudes for events comprising the pre-Darfield seismicity (pre-CES) and CES seismicity (CES) catalogues in relation to geodetically defined faults (Beavan et al., 2012). HAF = Hororata Anticline Fault; GF = Greendale fault; CCF = Charing Cross reverse fault; SKF = Sandy Knolls Fault.

April 2016; $M_w \geq 4.0$) and geological data (palaeoseismic recurrence interval of 20–30 kyr on the GF, as determined by Hornblow et al., 2014) to describe the magnitude-frequency distribution of the entire CES area as a G-R relationship and the GF area as best represented by characteristic earthquake behavior (Stirling & Zúñiga, 2017). They attributed these differences in earthquake scaling to variations in the size of the area analyzed and reported parameters of $b = 0.99 \pm 0.12$ and $M_c = 4$ (Stirling & Zúñiga, 2017).

2.3. Stress Drop

Average static stress drops ($\Delta\sigma$) for individual faults that ruptured in the Darfield earthquake were previously computed from seismic source models by Elliott et al. (2012) using the equation of Scholz (2002):

$$\Delta\sigma = 2M_o/\left(\pi W^2 L\right) \tag{1}$$

where M_o is the seismic moment, W is fault width, and L is fault length. Using the finite fault models of Beavan et al. (2012) and equation (1), we computed $\Delta\sigma$ for the faults in the Beavan model (Figure 3a). The results highlight how differences in source fault model dimensions and slip estimates influence $\Delta\sigma$ (Figure 3a). The average $\Delta\sigma$ for the Darfield earthquake using the Elliott et al. (2012) source model is 6.0 MPa and using the Beavan et al. (2012) source model is 3.9 MPa (Figure 3a).

Oth and Kaiser (2014) used source spectra derived from spectral inversion of strong ground motions to estimate seismologic stress drops $\Delta\sigma^s$ for 205 M_w 3 to 7.1 earthquakes recorded during the 2010–2011 CES (Figure 3b) following Hanks and Thatcher (1972):

$$\Delta\sigma^s = 8.5\, M_o\, \left(f_c/v_s\right)^3 \tag{2}$$

where f_c = corner frequency and v_s = crustal shear wave velocity (3.3 km/s). $\Delta\sigma^s$ for individual events ranges from 1.1 to 33.6 MPa with a median of 5 MPa and average of 6 MPa (Figure 3b). No M_w dependence or relationship to hypocentral depth or faulting mechanism was observed. The $\Delta\sigma^s$ for the Darfield earthquake was estimated at 5.7 MPa. The general consistency in independently derived $\Delta\sigma$ and $\Delta\sigma^s$ estimates suggests that the Darfield earthquake and its aftershocks are consistent with globally compiled median (6 MPa) $\Delta\sigma$ estimates from intraplate regions, and higher than global median interplate $\Delta\sigma$ estimates (3.3 MPa; Allmann & Shearer, 2009).

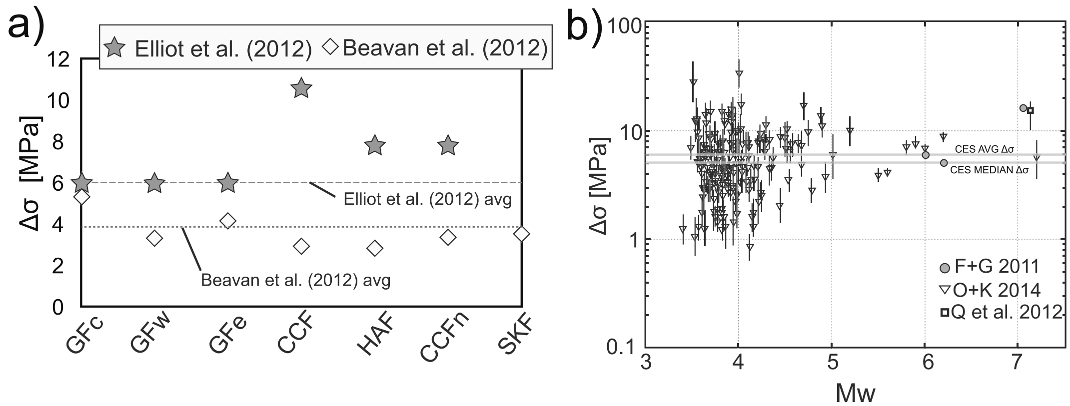

Figure 3. Stress drop estimates for the Canterbury earthquake sequence (CES). (a) Geodetically defined stress drops proposed for source faults. (b) Seismological stress drop versus magnitude relationship reported for events within the CES seismicity sequence (F+G 2011 = Fry & Gerstenberger, 2011; O+K 2014 = Oth & Kaiser, 2014; Q et al. 2012 = Quigley et al., 2012).

2.4. Utility of Stress Drop Estimates in Coulomb Static Stress Change Calculations

Static stress increases of <0.01 MPa to >1 to 1.5 MPa have been required to initiate fault rupture under some circumstances (Stein et al., 1997; Stein, 1999; Walters et al., 2018). Prerupture fault stress states (Harris & Day, 1999) and fault strength (Ben-Zion & Sammis, 2003; Ito et al., 2017) may be heterogeneous, creating further epistemic uncertainty as to what value of static stress change would theoretically be sufficient to initiate instantaneous rupture and whether this rupture (if initiated) would propagate across the entire receiver fault. Earthquake stress drops may be invariant with respect to earthquake magnitude and rupture size (Shaw, 2009), as evidenced in the CES data (Figure 3). Instantaneous stress drop on the hypocentral rupture patch of a commencing rupture may or may not vary significantly from the average stress drop once that fault has fully ruptured. The CSC added to a receiver fault could either exceed the subsequent stress drop (e.g., an “incomplete stress drop”), or the stress drop could exceed effective stress (e.g., “dynamic overshoot”; Madariaga, 1976).

Given these uncertainties, we consider a variety of different CSC thresholds (0, 1, 5, and 10 MPa) in the CSC models of the Darfield earthquake source faults. We assume that, if the stress change in at least one 1 × 1-km rupture patch exceeds threshold values (CSC_x^{crit}), spontaneous rupture is triggered and propagates across the entire fault (Beroza & Ellsworth, 1996; Dieterich, 1992; Madariaga, 1976). The lower bound (0 MPa) assumes that any positive static stress change (e.g., 0.01 MPa) initiates receiver fault rupture. The intermediate values (1, 5 MPa) are consistent with the lowest and median $\Delta\sigma^s$ estimates for the Darfield earthquake and its aftershocks (Oth & Kaiser, 2014) and consistent with rupture initiation CSC^{crit} in other fault systems (Walters et al., 2018). The 10 MPa is viewed as an upper limit, to allow for the possibility that this CSC change spatially coincided with a receiver fault patch that required a stress increase significantly (i.e., 2 times) larger than the average static stress drop for spontaneous rupture to initiate. These assumptions are discussed in more detail below.

3. Methods

3.1. Coulomb Stress Modeling of Multifault Rupture Scenarios

We use the finite fault source model and slip distributions of Beavan et al. (2012) and Coulomb stress modeling (King et al., 1994) to calculate Coulomb static stress changes (CSC) imposed by source fault ruptures onto proximal receiver faults (Figures 1 and 4). CSC values are calculated using Okada's (1992) equations. These equations derive the stress tensor from a set of dislocations in a half-space. After orientating the stress tensor onto the receiver fault, we can use the following formula to get the CSC value:

$$CSC = \Delta\tau + \mu\ (\Delta\sigma_n + \Delta \mathrm{P}) \tag{3}$$

where $\Delta\tau$ is the shear stress change along the strike direction, $\Delta\sigma_n$ is the normal stress change, μ is the friction coefficient, and ΔP is the pore pressure change. Positive values for the CSC bring the fault closer to

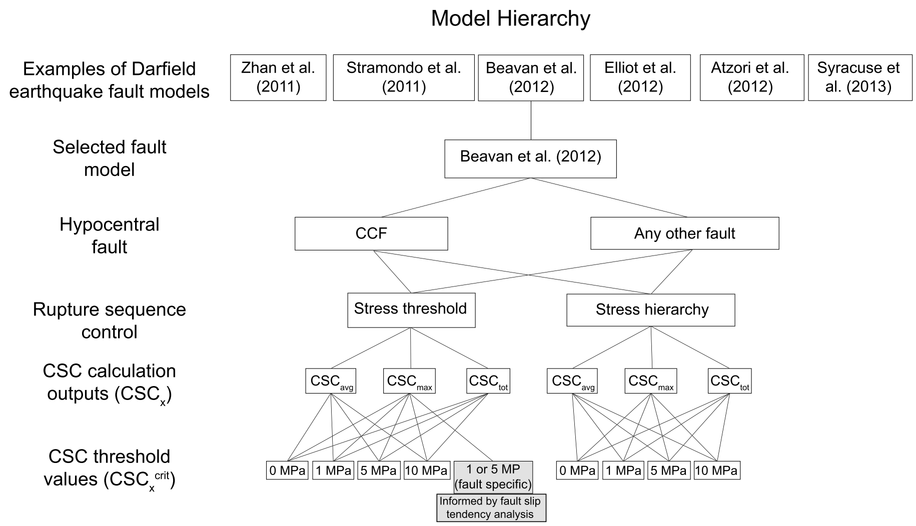

Figure 4. Branching model network hierarchy for CSC modeling (section 3.1) and simplified methodology of fault tendency analysis (section 3.2). CSC = Coulomb stress change; CCF = Charing Cross reverse fault.

failure, whereas negative values distance it from failure. Pore fluid pressure changes are usually assumed to be proportional to normal stress changes (Cocco & Rice, 2002), so an effective friction coefficient (μ') is used, with a value of 0.4 as the most representative for all fault orientations (King et al., 1994). This value for μ' corresponds to a hydrostatic gradient in pore pressure.

Among available Darfield earthquake models (Figure 4), we select the Beavan et al. (2012) model for our analysis for the reasons described above. We produce a large number ($n = 168$) of different CSC models that are represented using a branching model network to demonstrate how variations in the hypocentral fault identity and CSC-based criteria influence model results (Figure 4). At the "hypocentral fault" level we produce CSC models for rupture initiating on the CCF (as evidenced for the Darfield earthquake, see section 2.2) and models for rupture initiating on any of the other (non-CCF) faults in the network (seven different model families in total, represented by a single box in Figure 4 for simplicity). At the "rupture sequence control" level, the "stress threshold," criterion assumes instantaneous rupture occurs on any receiver fault if the imposed CSC is greater than the defined critical CSC value (CSC^{crit}), with subsequent recalculation of stress on unruptured receiver faults after each step. The second approach, "stress hierarchy," assumes only the receiver fault with the highest CSC value ruptures, and CSC values are then recalculated across the remaining receiver faults. Rupture ceases in both approaches when the imposed CSC on a receiver fault is $<CSC^{crit}$. The stress hierarchy approach has similar theoretical aspects to the rupture branching analysis conducted by Parsons et al. (2012). For all model families, the average CSC (CSC_{avg}), summative total CSC (CSC_{tot}), and maximum CSC (CSC_{max}) for any 1-km^2 fault pixel (Parsons et al., 2012) are calculated for all receiver faults ("CSC calculation outputs"). Whether rupture occurs for these different CSC values is then set by whether CSC_x (the CSC value considered) is greater than or equal to different "CSC thresholds" that are set to 0, 1, 5, or 10 MPa (Figure 4).

These CSC models all simplify what is undoubtedly a more complex process of rupture initiation and propagation. The assumption that fault rupture extents, slip magnitudes, and slip vectors on the faults will be consistent with the Beavan et al. (2012) model regardless of the order in which that fault ruptures is a major epistemic uncertainty that we do not investigate. The CSC_{max} threshold criteria are perhaps most consistent with a propagating crack model (Madariaga, 1976);however, the CSC^{crit} values for all models are theoretical (as discussed in section 2.4), based only on limited empirical evidence for CSC-triggered earthquakes and subject to large uncertainties.

To qualitatively assess which model and model parameters best replicate the expected behavior of this fault system, results from the hypocentral fault = CCF family of models (Figure 4) are evaluated to determine which model(s) best replicates the rupture order sequence independently proposed for the Darfield earthquake (Holden et al., 2011). This model(s) is thus assumed to best represent the rupture scenarios for ruptures initiating on other faults ("any other fault"). Given the abundance of epistemic uncertainties at this stage, we prefer a qualitative description of model outputs rather than a weighted logic tree approach (e.g., Scherbaum & Kuehn, 2011), although the latter approach could be utilized in future studies.

CSC results for all experiments are presented as raw outputs, static images and videos that are available at https://eartharxiv.org/v8t3n/ (DOI: 10.31223/osf.io/v8t3n). CSC results for the "CCF ➔ stress threshold ➔ CSC_{max}" model pathway for "CSC^{crit} = 0,1,5,10 MPa" are shown in Figures 5a–5c. Results for the "any other fault ➔ stress threshold ➔ CSC_{max}" pathways are shown for 1 MPa in Figures 5d–5i and 5 MPa in Figures 5j–5o.

3.2. Fault Slip Tendency Analysis

We used fault slip tendency analysis to assign different $CSC_{max}{}^{crit}$ values for different faults depending on their geometries (strike and dip) and slip kinematics (Beavan et al., 2012) (Figures 1 and 6). We set $S_{Hmax} = \sigma_1$ at an azimuth of 115° (Ellis et al., 2016; Sibson, Ghisetti, & Crookbain, 2012; Sibson, Ghisetti, & Ristau, 2011). The magnitude of the maximum principal stress σ_1 is given by the following:

$$\sigma_1 = \sigma_3 + \sigma_D \tag{4}$$

where σ_3 is the magnitude of the minimum principal stress $\sigma 3$ (vertical in a contractional regime) and σ_D is the magnitude of the regional differential stress. We estimate σ_3 at seismogenic depth (9 km) ≈ 236 MPa, based on 600 m of gravel cover (2,300 kg/m^3) over 8.4-km bedrock (2,700 kg/m^3). We use $\sigma_D \approx 130$ MPa (Ellis et al., 2016), which is consistent with the differential stress expected on a strike-slip fault operating at hydrostatic pore pressure (88 MPa) and following typical Byerlee friction (Zoback & Townend, 2001).

We estimate that the effective minimum and maximum principal stresses, after accounting for pore pressure, are $\sigma_3 \approx 148$ MPa and $\sigma_1 \approx 236 + 130–88 = 278$ MPa (Figure 6). We assume that $\sigma_1 > \sigma_2 \approx \sigma_3$ at seismogenic depths (i.e., stress ratio ≈ 1; Ellis et al., 2016; Herman et al., 2014; Sibson, Ghisetti, & Ristau, 2011) and resolve the calculated stresses at 9-km depth onto each of the seismogenic fault planes using FaultKin8 software (Allmendinger et al., 2012; Marrett & Allmendinger, 1990). We then calculate slip tendency as the ratio of the shear stress to the normal stress τ/σ_N (Figure 6a).

Using these stress estimates and a static friction coefficient of 0.6, a fault oriented at the potential lock-up angle (60°; Figure 6b) would have $\tau/\sigma_N = 0.23$ (Figure 6a). We therefore separate the faults into those with "high" slip tendency ($\tau/\sigma_N > 0.23$) and "low" slip tendency ($\tau/\sigma_N < 0.23$; Figures 6a and 6c and Table 1). For our Coulomb stress model pathways "stress threshold ➔ CSC_{max}" (see section 4.1 for details on these model choices), high slip tendency faults were assigned a $CSC_{max}{}^{crit}$ of 1 MPa (optimally orientated for rupture); low slip tendency faults were assigned a $CSC_{max}{}^{crit}$ of 5 MPa (misorientated for rupture).

3.3. Derivation of Seismicity Frequency-Magnitude Distributions

We analyze seismicity during the CES ("CES seismicity catalogue"; 3 September 2010 to 31 May 2017 UTC) and the 60 years prior to the Darfield earthquake ("pre-Darfield seismicity catalogue"; 3 September 1940 to 2 September 2010). Seismological data were downloaded from the GeoNet earthquake catalogue (https://quakesearch.geonet.org.nz/; accessed 13 June 2017) for hypocenters ≤12 km deep within the region encompassing the Darfield earthquake source faults (see GR window; Figure 2). The 12-km depth limit reflects the maximum depth of Darfield earthquake source fault ruptures estimated by Beavan et al. (2012).

All events in the CES seismicity catalogue (n = 4,312: 3163 $M_L \geq 2.6$ and 94 $M_w \geq 2.6$) are reported in local magnitude (M_L). We assume $M_w \approx M_L$ because M_w to M_L conversions for small magnitude events are highly uncertain and the small (2.9%) contribution of M_w events to the total data set does not influence counting statistics beyond the bounds of the uncertainties reported. The catalogues also contain a mix of manually relocated hypocentral depths and operator-assigned depth estimates that are assigned to either 5 km (n = 3,204) or 12 km (n = 163). Comparison of a subset of CES events assigned a 5-km hypocentral depth, with Syracuse et al.'s (2013) relocated hypocenters indicates that they all occurred at less than 12-km depth and thus fit the criteria for inclusion in this catalogue. The events assigned a 12-km depth are generally low magnitude (only five events exceed M_L 3.7, and none exceed M_L 4.2), so potential errors in event populations at depth = 12 km do not introduce significant error to the data set.

10.1029/2019JB017508

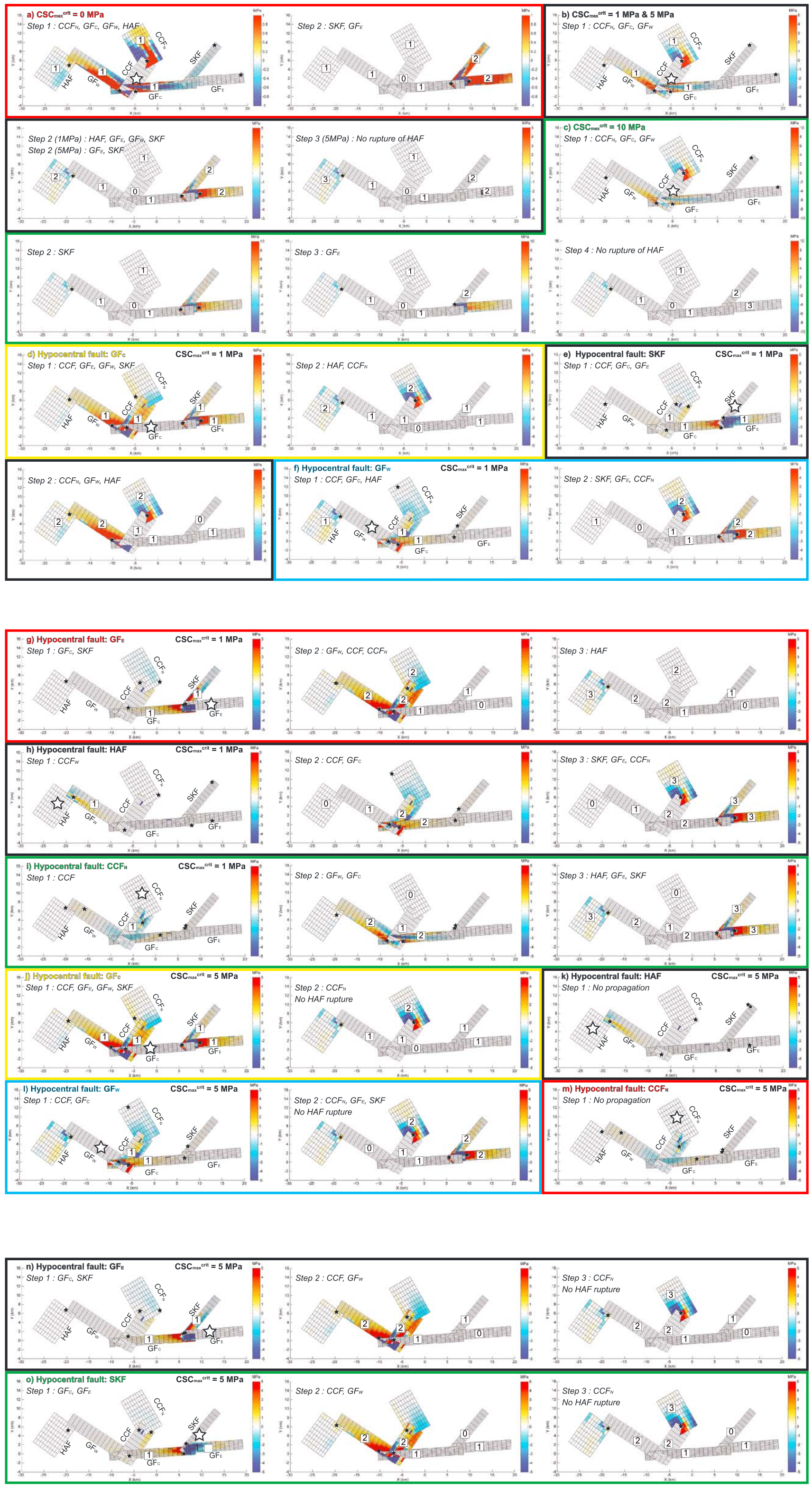

Figure 5. (a–c) Coulomb stress change (CSC) modeling results for “stress threshold ➔ CSC_{max} ➔ 0 to 10 MPa” rupture scenarios initiating on the Charing Cross reverse fault (CCF), showing steps involved in each model. The scale varies per model to highlight CSC_{max}^{crit} values. (d–i) CSC modeling results for “stress threshold ➔ CSC_{max} ➔ 1 MPa” with different hypocentral rupture scenarios. (j–o) CSC modeling results for “stress threshold ➔ CSC_{max} ➔ 5 MPa” with different hypocentral rupture scenarios.

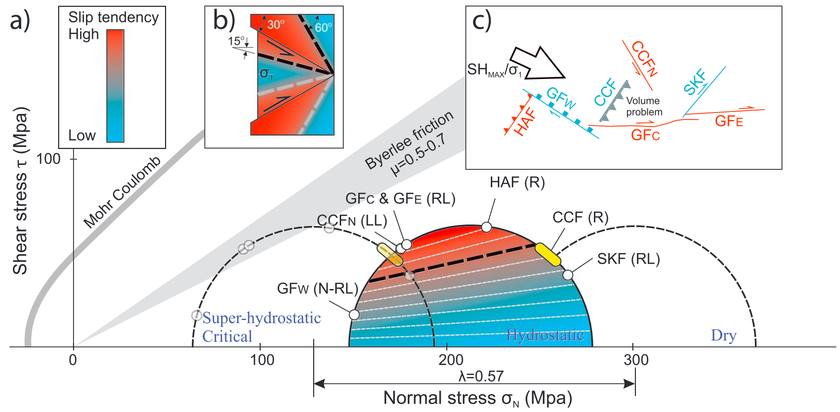

Figure 6. (a) Mohr diagram of fault slip tendency and stress states calculated for hydrostatic pore pressure at 9-km depth (colored circle) for the Darfield earthquake source faults, based on geometry of Beavan et al. (2012; see section 3). Heavy dashed black line separates faults with high and low slip tendency and corresponds to lock-up fault dips of 15° and 60° (see inset b). Dashed circles show equivalent dry conditions (right), and fluid overpressure (pore fluid factor ≈0.57—left) required to initiate slip on optimally oriented faults within the network, obeying Byerlee Friction. CCF (yellow) shown with dip between 65° and 70°. (b) Fault map with faults color coded by sensitivity. Note that misoriented faults, including the progenitor CCF, remain stable when optimally oriented faults are already critically stressed. Fault abbreviations as Figure 1; N = normal; LL = left lateral; RL = right lateral; R = reverse. HAF = Hororata Anticline Fault; CCF = Charing Cross reverse fault; SKF = Sandy Knolls blind fault.

We use a minimum magnitude of completeness (M_c) for shallow seismicity following Zúñiga et al. (2005) of $M_c = 4.4$ for the interval 1940 to 1968; $M_c = 3.9$ for the interval 1968 to 1987; and $M_c = 2.6$ for 1987 to 2010. Only 11 of 25 $M_L \geq 2.4$ earthquakes from the pre-Darfield catalogue passed the Zúñiga et al. (2005) M_c test and fit the depth criteria. The spatial (Figure 2) and temporal dispersion of these events indicates that they are independent events (i.e., they should not be filtered using declustering algorithms). All hypocentral depths in the Pre-Darfield catalogue were fixed at 5 or 12 km due to poor depth control. However, only two earthquakes occurred at the shallower depth and the only $M_L \geq 4.0$ earthquake was assigned a depth of 12 km, although it may have been deeper. Thus, depending on the M_c and depth criteria used (both of which are epistemically uncertain), 0 to 11 events comprise the pre-Darfield seismicity catalogue. The inherent incompleteness of this catalogue introduces uncertainties in frequency-magnitude a and b values (Figure 7b) that we discuss in more detail in section 5.3.

We fit earthquake frequency-magnitude data for pre-Darfield and CES catalogues following Woessner and Wiemer (2005), where earthquake distributions for $M_L < M_c$ are modeled as a cumulative Gaussian

Table 1
Results of Slip Tendency Analysis

Fault	Strike (deg)	Dip (deg)	Trace length (km)	Sense of slip	D_{av}	D_{max}	Shear stress τ	Effective normal stress σ_N	Effective slip tendency τ/σ_N	Slip azimuth (model)	Slip plunge (model)	Slip azimuth (calc)	Slip plunge (calc)	shear stress-slip mismatch°
GF_E	86	78	13	RL	1.94	5.59	54	177	0.31	86	2	87	6	5
GF_C	86	80	19	RL	2.84	7.58	55	178	0.31	87	6	87	5	0.5
CCF_N	150	54	9	LL	1.34	2.50	53	176	0.3	326	5	316	18	16
HAF	216	50	8	Rev	1.12	3.96	64	222	0.29	324	49	281	47	28
CCF	35	70	9	RLRev	1.22	5.64	46	259	0.18	93	67	69	57	15
SKF	40	80	12	RL	1.44	3.34	38	266	0.14	42	9	46	32	24
GF_W	303	75	16	N	1.82	4.60	17	150	0.11	119	14	122	2	13

Note. See text for methodological details. Fault strike, dip, trace length, slip sense, D_{av}, D_{max}, slip azimuth (model), and slip plunge (model) are from the finite fault model of Beavan et al. (2012). See Beavan et al. (2012) for rake. Slip azimuth (calc) and slip plunge (calc) are derived from the calculated direction of maximum shear stress (this study); the difference in rakes between the (model) and (calc) slip models is reported in the shear stress-slip mismatch column. GF_W = Greendale fault west; SKF = Sandy Knolls blind fault; CCF = Charing Cross reverse fault; HAF = Hororata Anticline Fault; CCF_N = Charing Cross north fault; GF_C = central section of the strike-slip Greendale fault; GF_E = strike-slip Greendale fault east.

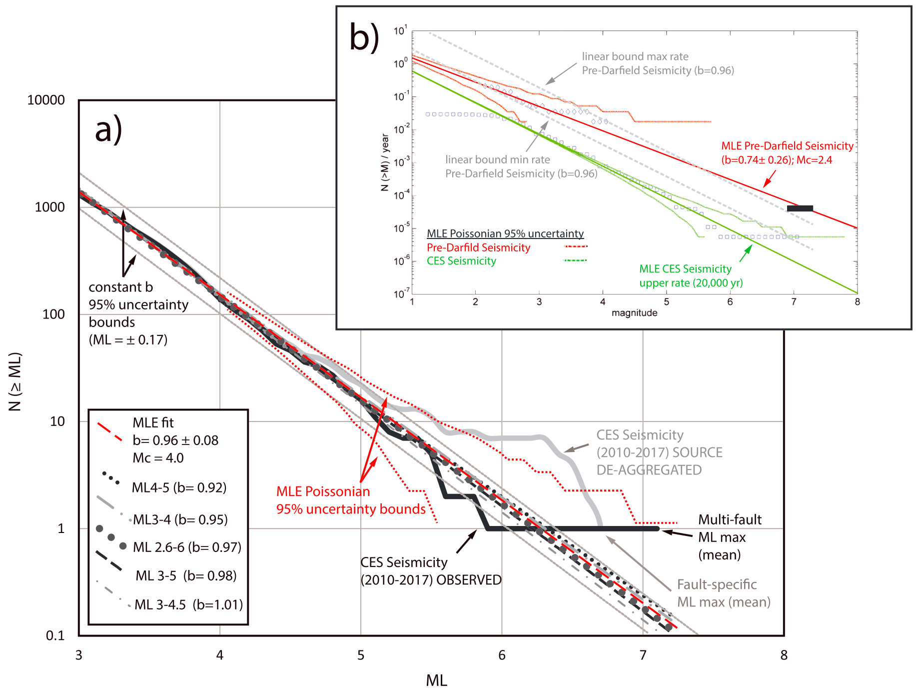

Figure 7. (a) Darfield earthquake and associated aftershocks (Canterbury earthquake sequence, CES, seismicity) frequency-magnitude plot showing maximum likelihood estimation (MLE) fit and incremental least squares b value fits to the data. Linear projections using MLE b value estimations to higher magnitudes reveals deviations from observed earthquakes (black line) and source magnitude deaggregated distributions (gray line). The 95% Poisson confidence intervals are shown. M_L maximums are derived for multifault earthquakes and source-specific earthquakes (i.e., the M_L max of a defined fault). (b) Earthquake annual rates versus M_L for the Darfield-aftershock data and pre-Darfield seismicity (pre-Darfield) data averaged over 20,000 years. Black box represents the annual rate estimate of Darfield-earthquake type events on the fault system (M_L 7.1 ± 0.2; recurrence interval 20,000 to 30,000 years); this resides beyond the upper limits of the 95% confidence bounds. Projection of the MLE-derived fit to the pre-Darfield Seismicity annual rate data to upper magnitudes intersects the Darfield earthquake recurrence; however, we have low confidence in the associated b value. Assumption of $b = 0.96$ (the value of the MLE fit to the CES seismicity data) and adjustment of a to fit the upper bounds of the pre-Darfield seismicity rate provides another intersecting fit to the Darfield earthquake recurrence box. Neither the Gutenberg-Richter hypothesis nor characteristic earthquake hypothesis for the near source region of the Darfield earthquake can be statistically defended.

distribution and for $M_L \geq M_c$ they are modeled as an exponential. The exponential part is used to derive b values according to maximum likelihood estimation (MLE; Aki, 1965), corrected for minimizing binning effects (Utsu, 1966). We also show 95% confidence bounds derived from the inverse Poisson function (Naylor et al., 2009).

In Figure 7a we show a hypothetical frequency-magnitude catalogue that includes all CES events but also separates the Darfield earthquake into a seven distinct earthquakes with M_L contributions based on Beavan et al.'s (2012) fault-specific M_o estimates. This is akin to "deaggregating" this single earthquake into several earthquakes with individual magnitudes corresponding to the magnitude of earthquakes emanating from individual faults in the network. We do not deaggregate any of the aftershocks because there is no evidence for multifault contributions to aftershocks within our spatial domain (although we cannot dismiss this possibility).

Following the method described in Stirling and Zúñiga (2017), we apply the rates of CES seismicity to a 20,000-year time period (the minimum expected recurrence interval range of GF surface rupturing earthquakes (20–30 kyr; Hornblow et al., 2014) assuming no future aftershocks and no pre-Darfield seismicity (Figure 7b; CES seismicity). Average annual rates of less than three $M_L = 3.6$ earthquakes averaged over the 1 January 2016 to 31 May 2017 window are still 84 to 8 times greater than annual rates from the pre-Darfield seismicity model (in accordance with Omori's law following the Darfield earthquake and

10.1029/2019JB017508

large aftershocks; Gerstenberger et al., 2014; Quigley & Forte, 2017; Shcherbakov et al., 2012), suggesting that the CES aftershock sequence is still ongoing.

Annual seismicity rates and *b* values for the CES (extrapolated over 20,000 years and assuming no pre-CES and no additional seismicity) and pre-Darfield catalogues are derived using MLE with 95% Poissonian error bounds (Figure 7b). We also project central linear fits to upper magnitudes to compare these estimations with the annual rate of M_w 7.1 ± 0.2 earthquakes on the GF from Hornblow et al. (2014; Figure 7b). For illustrative purposes, maximum and minimum rate-bounded linear fits to the pre-Darfield seismicity derived using the *b* value from the CES catalogue ($b = 0.96$) are also shown, based on the previously reported observation that frequency-magnitude distributions in the broader Canterbury earthquake region prior to the Darfield earthquake follow $b = 0.97$ (Quigley et al., 2016) and appear to be statistically indistinct from the CES *b* values reported herein.

4. Results

4.1. Coulomb Stress Modeling of Multifault Rupture Scenarios

The modeling approach and results for 168 CSC models, including static images and videos, is published in Quigley et al. (2018). We synthesize the key findings below.

4.1.1. CCF Rupture Initiation

In the s*tress threshold* ➔ CSC_{max} ➔ CCF hypocenter models (Figures 5a–5c), CCF rupture causes rupture propagation on CCF_N, GF_C, and GF_W for $CSC_{max}{}^{crit}$ = 0 to 10 MPa, consistent with Holden et al. (2011). HAF ruptures instantaneously in step 1 when $CSC_{max}{}^{crit}$ = 0 MPa (Figure 5a, step 1), ruptures in Step 2 for $CSC_{max}{}^{crit}$ = 1 MPa, but does not rupture in models with $CSC_{max}{}^{crit}$ = 5 and 10 MPa because HAF CSC_{max} = 1.5 MPa. SKF and GF_E rupture in step 2 for $CSC_{max}{}^{crit}$ = 0 to 5 MPa, and in steps 2 and 3, respectively, in $CSC_{max}{}^{crit}$ = 10 MPa. The Holden et al. (2011) sequence is best described by a combination of the $CSC_{max}{}^{crit}$ = 1- and 5-MPa models; the HAF should be the last in the sequence to remain following rupture of other receiver faults (consistent with the $CSC_{max}{}^{crit}$ = 5-MPa sequence) but must ultimately rupture (consistent with the $CSC_{max}{}^{crit}$ = 1-MPa model results). We explore this further in section 4.2.

For *stress threshold* ➔ CSC_{avg} ➔ CCF models (Quigley et al., 2018), rupture propagates from the CCF on to other faults in the system only when $CSC_{avg}{}^{crit}$ = 0 MPa. CCF_N and GF_W rupture in step 1, followed by SKF (step 2). GF_C, GF_E, and HAF do not rupture. This family of models does not adequately represent the Darfield earthquake sequence (Holden et al., 2011) and is thus not discussed further. For *stress threshold* ➔ CSC_{tot} ➔ CCF models, spontaneous rupture (step 1) occurs on the CCF_N and GF_W for all (0 to 10 MPa) $CSC_{tot}{}^{crit}$ values. Rupture then continues onto the SKF (step 2) for $CSC_{tot}{}^{crit}$ = 0, 1, and 5 MPa (not 10 MPa). GF_C, GF_E, and HAF do not rupture in any models. This family of models does not adequately represent the Darfield earthquake sequence (Holden et al., 2011) and is thus not considered further. Full results are presented in Quigley et al. (2018).

Within the *stress hierarchy* ➔ CSC_{max} ➔ CCF models (Quigley et al., 2018) full rupture of the fault system occurs at $CSC_{max}{}^{crit}$ = 0 and 1 MPa. At $CSC_{max}{}^{crit}$ = 5 and 10 MPa, the HAF is the only fault does not rupture. The rupture order for all models is CCF then CCF_N, GF_C, GF_W, SKF, GF_E, and finally HAF (0 and 1 MPa only). The 0- and 1-MPa models represent the generalized rupture order of Holden et al. (2011) model well (CCF rupture spreading first to intersecting, interior faults and finishing with rupture of distal faults at the periphery of the network) and thus warrant further discussion (next paragraph). None of the *stress hierarchy* ➔ CSC_{tot} or CSC_{avg} ➔ CCF models successfully rupture all faults. Under $CSC_{avg}{}^{crit}$ = 0 MPa and $CSC_{tot}{}^{crit}$ = 0, 1, and 5 MPa, the rupture order is CCF, GF_W (step 1), GF_E (step 2), and SKF (step 3). GF_C, GF_E, and HAF fail to rupture across all CSC_{tot} and CSC_{avg} models; the inadequacy of these models to replicate the Darfield earthquake rupture excludes the need to discuss them further in this paper.

While we cannot dismiss the potential importance of fault-averaged (CSC_{avg}) or fault-total CSC changes (CSC_{tot}) in earthquake sequences elsewhere, application of these criteria does not successfully replicate the key elements of the observed Darfield earthquake sequence and thus these criteria are inadequate in this regard. The *stress hierarchy* ➔ CSC_{max} ➔ CCF models replicate aspects of the proposed rupture order for the Darfield earthquake based on seismologic and geodetic data (Holden et al., 2011). However, the philosophical underpinning for this approach is suspect because the Darfield earthquake initiated on a source fault

(CCF) with connections at either end of the rupture (CCF_N and $GF_C + GF_W$) and so the propagating rupture did not need to "make a choice" among fault branches; both branches could (and did) rupture. Furthermore, the body wave source time function (15 s; Elliot et al., 2012) and duration of rupture time in the Holden et al. (2011) model (18 to 20 s) for the Darfield earthquake are inconsistent with the time it would take to release seismic energy from distinct, sequential ruptures of the Darfield earthquake source faults (86 km with rupture speed of ~2 to 2.5 km/s = 35 to 43 s). This suggests that concurrent ruptures spread on to multiple branching faults in a bilateral manner during the earthquake, consistent with the *stress threshold* ➔ CSC_{max} ➔ CCF hypocenter models for $CSC_{max}{}^{crit} = 1$ and 5 MPa.

4.1.2. Any Other Fault Rupture Initiation

Given the success of *stress threshold* ➔ $CSC_{max}{}^{crit} = 1$- and 5-MPa models to replicate the Holden et al. (2011) model, we now apply these conditions to other rupture scenarios, where the earthquake initiates on a different hypocentral source fault (Figures 5d–5o). At $CSC_{max}{}^{crit} = 1$ MPa, earthquakes beginning on GF_C (Figure 5d), SKF (Figure 5e), GF_W (Figure 5f), GF_E (Figure 5g), HAF (Figure 5h), and CCF_N (Figure 5i) all progress to complete system rupture in two steps (ruptures commencing on faults in the network interior; CCF, GF_C, GF_W, and SKF) or three steps (ruptures beginning at the extremities of the network; HAF, CCF_N, and GF_E). At $CSC_{max}{}^{crit} = 5$ MPa, rupture occurs across the entire fault network excluding HAF for ruptures initiating on the GF_C (three steps; Figure 5j), GF_W (three steps; Figure 5l), GF_E (four steps; Figure 5n), and SKF (four steps; Figure 5o). The HAF does not rupture because CSC_{max} is 1.5 to 1.6 MPa in these scenarios. Earthquakes initiating on the HAF (Figure 5k) and CCF_N (Figure 5m) do not propagate beyond the hypocentral fault. This suggests that, depending on which fault in the network ruptures first (hypocentral fault) and which stress threshold is selected, rupture cascades may or may not occur across the system. This is investigated further below.

4.2. Fault Slip Tendency Analysis and Integration With CSC Models

We quantify the stability and slip tendencies of all Darfield system faults within the regional stress field (Ellis et al., 2016; Herman et al., 2014; Sibson, Ghisetti, & Crookbain, 2012) using slip tendency analysis. Results are provided in Table 1 and Figure 6. The E-W dextral strike-slip faults (GF_C and GF_E), their conjugate NW-SE sinistral fault (CCF_N) and the relatively low angle thrusting HAF all have high slip tendencies ($\tau/\sigma_N < 0.2$). The CCF, SKF, and GF_W have comparably low slip tendencies ($\tau/\sigma_N < 0.2$). Slip tendencies are shown in relation to the Mohr-Coulomb fracture criterion for New Zealand greywackes using criterion based on McNamara et al. (2014), with a conservative tensile strength for South Island greywacke adopted from Stewart (2007; Figure 6). If faults with highest slip tendencies are assumed to obey Byerlee friction ($\mu = 0.5$–0.7), the strike-slip faults and the HAF must have been either frictionally stronger than the CCF by a factor of 2, or initial rupture was triggered by a transient pore pressure increase of up to 120 MPa that affected the CCF and GF_W but did not affect other faults within distances of <1 to 10 km. Vast differences in frictional strength or pore pressures across these short distances offer improbable explanations for the observed rupture sequence (Fletcher et al., 2016b). We explore this in more detail in Section 5.

We combine our fault slip tendency analysis with the *stress threshold* ➔ CSC_{max} models to investigate how fault system geometry and stability affect rupture scenarios in the Darfield fault system. We assign $CSC_{max}{}^{crit} = 1$ MPa for faults with a high slip tendency (GF_E, GF_C, CCF_N, and HAF) that are optimally orientated with regional crustal stresses. For misoriented faults with low slip tendency (CCF, SKF, and GF_W) we assign $CSC_{max}{}^{crit} = 5$ MPa (Figures 6 and 8). As described in section 2.4, these values are consistent with seismogenic stress drop for the Darfield sequence (Oth & Kaiser, 2014; Figure 3). For the Darfield earthquake simulation (CCF hypocentral fault), all source faults rupture by step 2 and the predicted rupture sequence matches the seismologically observed sequence, with late-stage HAF, GF_E, and SKF ruptures (Figure 8b). For GF_C, GF_W, and SKF hypocentral scenarios, all source faults rupture by step 2 (Figures 8b and 8c). The GF_E hypocentral fault ruptures all other faults by step 3. For all these scenarios, the multifault earthquake is equivalent to M_w 7.1 (Figure 8d), consistent with the Darfield earthquake. Earthquakes initiating on the HAF and CCF_N, despite those faults being optimally orientated, do not propagate beyond the source fault because adjacent receiver faults are highly misoriented and thus have higher $CSC_{max}{}^{crit}$ values (Figure 8c). The M_w of these scenario earthquakes (M_w 6.3) is limited by the size and slip distributions of the HAF and CCF_N (Figure 8d).

10.1029/2019JB017508

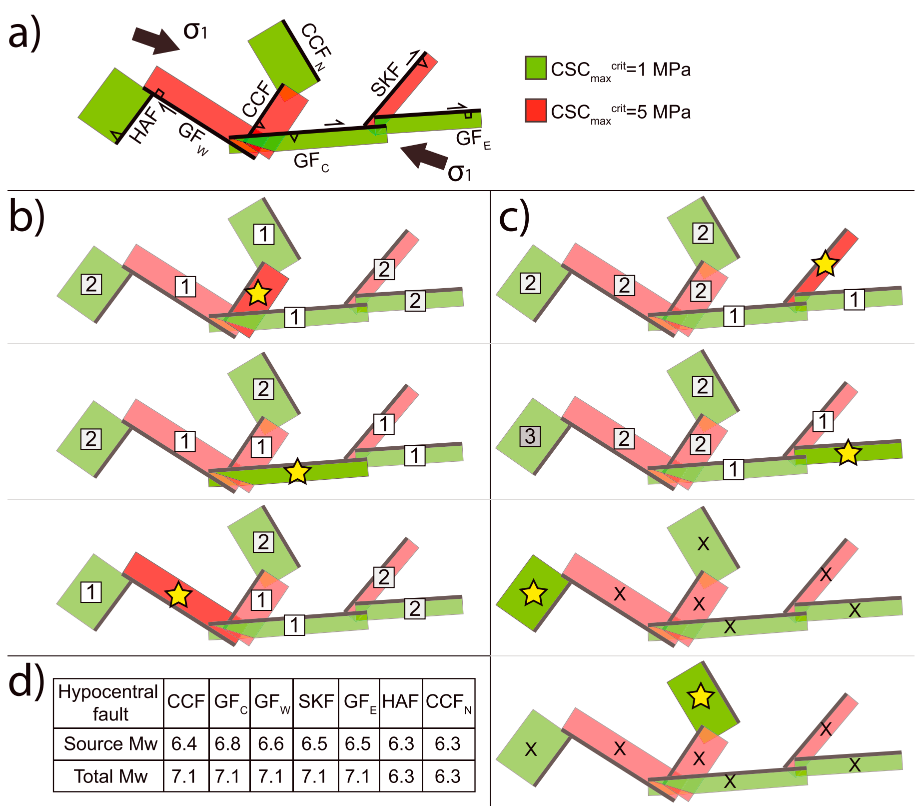

Hypocentral fault	CCF	GF_C	GF_W	SKF	GF_E	HAF	CCF_N
Source Mw	6.4	6.8	6.6	6.5	6.5	6.3	6.3
Total Mw	7.1	7.1	7.1	7.1	7.1	6.3	6.3

Figure 8. (a) Geometric arrangement of the Darfield earthquake source faults colored for assigned $CSC_{max}{}^{crit}$ values. (b) Sequence of fault failure for fault-slip tendency informed CSC modeling scenarios with hypocentral faults interior to the system. (c) Sequence of fault failure for fault-slip tendency informed CSC modeling scenarios with hypocentral faults exterior to the system. (d) Individual sources with defined M_w (source M_w) amalgamated into larger M_w (total M_w) for every hypocentral fault scenario (total M_w > source M_w). HAF = Hororata Anticline Fault; GF = Greendale fault; CCF = Charing Cross reverse fault; SKF = Sandy Knolls blind fault.

The Darfield earthquake provides empirical evidence for a cascading multifault earthquake initiating on a misoriented fault. However, it is unknown whether the fault system consistently ruptures with initiation on the CCF, or if other faults have previously initiated multifault rupture. Our geologically and seismologically informed CSC models (Figure 8) demonstrate that if equal probability is assigned to a hypocentral fault location on any fault within the network, 71% of earthquakes are predicted to cascade across the entire fault network (M_w 7.1), and 29% of earthquakes terminate within the hypocentral source fault (M_w 6.3). It is possible that the HAF and CCF_N faults have different slip rates and recurrence intervals from the other source faults, due to the geometric constraints imposed by neighboring faults that inhibit rupture propagation. We investigate this further below.

4.3. Frequency-Magnitude Distributions and b Value Estimations

Earthquake frequency-magnitude distributions in the CES Seismicity catalogue adhere to G-R scaling with MLE-derived values of $b = 0.96 \pm 0.08$ and $M_c = 4$ (Figure 7a). These estimates are consistent with previously reported analyses ($b = 0.99 \pm 0.12$, $M_c = 4$; Stirling & Zúñiga, 2017) with the variation attributable to small differences in the area, depth restrictions, and time intervals analyzed.

The b values for CES seismicity obtained using Gaussian least squares fits to different M_L ranges between 2.6 and 6 yield central values that are confined within the bounds of the MLE-derived b value Poissonian 95% uncertainty estimates (although the MLE method is preferred). Including Gaussian 95% confidence bounds that could result from uniform systemic errors in seismologically derived M_L estimations (assuming constant b values) produces hypothetical frequency-magnitude distributions that are confined at $M_L \geq 4.8$ within the MLE-derived 95% Poissonian confidence bounds to the observed data (Figure 7a). Determining b values using standard least squares regression with Gaussian residuals, especially in the case of log counts, may be susceptible to positively biased counting errors at larger magnitudes in earthquake frequency-magnitude tail distributions (Naylor et al., 2009; Sandri & Marzocchi, 2007) or negatively biased counting errors at low magnitudes, due to catalogue incompleteness. Both end-members have the potential to decrease b values and increase counting residuals if included in frequency-magnitude analysis. However, in this case, we demonstrate that simplistic Gaussian least squares fitting of different M_L-bounded frequency-magnitude data subsets for M_L 2.6 to 6 earthquakes in the CES catalogue provides b value estimates that reside within the 95% confidence bounds of the MLE-derived frequency-magnitude distribution and b value (Figure 7a). Consideration of statistical errors in M_L estimations that affect M_L-specific populations still yield Gaussian-derived frequency-magnitude distributions and b values that are confined within the Poissonian error distributions (e.g., $M_L \pm 0.17$ is shown for $b = 0.98$ in Figure 7a).

The CES catalogue with the Darfield earthquake magnitude deaggregated into fault-specific magnitudes (Figure 7a) generates a population of earthquakes with $5.8 \leq M_L \leq 6.6$ that outlie the MLE-derived 95% Poissonian confidence bounds defined by fits to the observed CES seismicity. M_w max in the observed data is represented by the Darfield earthquake (M_w 7.1) and M_w max in the deaggregated catalogue is equivalent to M_w 6.8 (the GF_C-specific M_w; Beavan et al., 2012).

Following Stirling and Zúñiga (2017) we derive a seismicity rate using CES earthquakes extrapolated over 20 kyr (Hornblow et al., 2014), assuming no additional aftershock inputs beyond the end of the analytical period (June 2017) and no premainshock or background seismicity. This produces annual seismicity rates with a "maximum" frequency-magnitude distribution and Poissonian 95% confidence bounds that are well below the expected annual rate of recurrence of M_w 7.1 $\pm$ 0.2 earthquakes from the paleoseismic data (Figure 7b), consistent with Stirling and Zúñiga's (2017) hypothesis for "characteristic" Darfield earthquakes. However, the observed pre-Darfield seismicity rate is higher than this extrapolated CES seismicity rate for the same M_L range. The data sparseness and poor statistical adherence of the pre-Darfield seismicity rates to G-R scaling, as manifested by a low precision b value ($b = 0.74 \pm 0.26$) with large 95% confidence bounds in frequency-M_L distributions, includes a lower bound that encompasses CES seismicity rate estimations. This indicates that the a and b values that define the pre-Darfield seismicity catalogue frequency-magnitude distribution cannot be statistically distinguished from the extrapolated CES seismicity catalogue values. The intersection of the MLE-derived pre-Darfield seismicity frequency-magnitude distribution with the geologically expected recurrence interval range of M_L 7.1 $\pm$ 0.2 earthquakes means that the proposed characteristic earthquake recurrence model for this area (Stirling & Zúñiga, 2017) cannot be proven against the alternative hypothesis (i.e., that near-source frequency-magnitude distributions follow G-R relationships). This is further evidenced by statistically indistinct $b \approx 1$ regional values for pre-Darfield seismicity and CES seismicity (Quigley et al., 2016). Shifting the a values for $b = 0.96$ (this study) to generate linearized fits through the upper and lower M_L rates from background seismicity creates linear interpolations that either intersect (i.e., G-R) or are significantly lower than (i.e., characteristic) the geologically estimated M_L 7.1 $\pm$ 0.2 rate (Figure 7b).

5. Discussion

5.1. CSC-Driven Multifault Rupture Cascade During the Darfield Earthquake

Dynamic rupture on fault networks is inherently complex. Rupture simulations and seismic observations indicate important effects of preexisting stress distributions, rupture propagation velocity, dynamic slip distributions, and dynamic triggering that can influence whether ruptures terminate at fault junctions or propagate onto neighboring faults (Bhat et al., 2004; Douilly et al., 2015; Freed, 2005; Harris & Day, 1993; Kame & Yamashita, 2003; Oglesby et al., 2008; Templeton et al., 2009; Templeton et al., 2010). In the first component of this study, we asked the question, *can CSC-modelling successfully replicate the multi-fault rupture sequence for the Darfield earthquake?* We addressed this question by producing an array of models that implement different measures of CSC values (maximum, average, and total) and rupture propagation criteria (CSC^{crit} between 0 and 10 MPa). We integrated CSC model results with independently derived seismologic (i.e., stress drop) and geologic (i.e., slip tendency) parameters. Our results (Figures 5, 6, and 8) indicate that a CSC model that integrates the largest volume of geological and seismologic data (${CSC_{max}}^{crit}$ = 1 MPa for optimally oriented faults and =5 MPa for misoriented faults) successfully simulates the published rupture sequence model of Holden et al. (2011) and offers explanations for some intriguing aspects of the Darfield earthquake, including strong ground motions and spatiotemporal variations in seismic moment release.

Our interpretations represent generalized models of a highly complex system. Because we do not quantitatively investigate the potential influences of variations in preexisting stress distributions (Lu, 2017), rupture velocities, slip distributions, and dynamic triggering stresses, we consider each of these to contribute epistemic uncertainties to our interpretations. We are unable to dismiss the possible role of these and other rupture characteristics and processes. However, the available data for this earthquake best reconcile our hypotheses that static stress perturbations during progressive fault rupture in the Darfield earthquake enabled the hypocentral fault rupture to spread coseismically across multiple faults with different slip tendencies.

Epistemic uncertainties in our data sets and analysis include (i) the validity of mainshock and aftershock stress drops (each with their own aleatoric uncertainties) used to inform reasonable values for CSC_{max}^{crit}, (ii) whether the Beavan et al. (2012) source model is the most accurate and precise representation of the source fault geometry, size, and slip distributions in the Darfield earthquake (and thus whether our CSC model estimates are robust), (iii) whether the Holden et al. (2011) rupture model accurately simulates the sequential rupture order of the Darfield earthquake (and thus whether the CSC-driven model replications successfully replicate the actual rupture process), (iv) whether the source-specific finite slip magnitudes and vectors used in CSC modeling are internally controlled by the host fault or whether they are codependent on the rupture of neighboring faults (and thus whether the incremental CSC model approach is a valid representation of the actual rupture process and resultant incremental CSC distributions), and (v) whether fault rupture tendencies are further complicated by unknown variations in intrinsic fault zone properties such as pore-fluid pressures, fault zone petrologic heterogeneity, and frictional properties (and thus whether the proposed assignment of source-specific CSC_{max}^{crit} estimates based on fault geometry alone adequately represents variations in fault slip tendency). A statistical treatment of each of these uncertainties is well beyond the scope of our study. However, we attempt to conservatively integrate them into our analyses in two simplistic ways (i) we assume that the Beavan et al. (2012) and Holden et al. (2011) models are the best (available) model representations of the source and dynamics of the Darfield earthquake and thus provide the best inputs to utilize in CSC modeling, and (ii) we conduct our CSC experiments using a large range of CSC_{max}^{crit} values (0 to 10 MPa). The integration of dynamic stresses and other processes in future work might enable further evaluation of this hypothesis.

5.2. Importance of Hypocentral Source Fault Characteristics on Multifault Rupture Cascades, Earthquake Maximum Magnitude, and Orogenic Growth of the Southern Alps, New Zealand

The 4 September 2010 M_w 7.1 Darfield earthquake and its two largest aftershocks (M_w 6.2 and 6.0) were sourced from multifault ruptures with hypocenter locations at (or near) junctions between highly oblique faults (Figure 1; Beavan et al., 2012). Fault slip maxima are concentrated in the central regions of individual faults (i.e., fault centroids) that are obliquely oriented with respect to neighboring faults (e.g., HAF, CCF, CCF_N, and SKF). Slip maxima occur at significant distances (≥4 km; equivalent to ≈1/2 of the fault lengths) from the hypocenter locations for all modeled $M_w \geq 6$ earthquakes during the CES (Beavan et al., 2012), consistent with global compilations of source models (Mai et al., 2005). This suggests that slip distributions on individual faults were primarily controlled by the geometry, area, and kinematics of the fault rupture rather than hypocenter location. Slip gradients are observed at fault junctions with greater kinematic linkage (manifested as slip vector continuity) and lower geometric obliquity with neighboring faults (e.g., GF_W-GF_C-GF_E). Collectively, these observations support our use of coseismic displacements observed in the Darfield earthquake to simulate ruptures initiating on faults other than the CCF for investigating how different hypocentral faults may or may not favor rupture propagation across the entire fault system.

Our results indicate that, (i) for CSC_{max}^{crit} thresholds of 0 and 1 MPa, ruptures cascade across the entire fault system irrespective of which fault acts as the hypocentral source, (ii) for CSC_{max}^{crit} thresholds of 5 and 10 MPa (i.e., greater than independently derived median $\Delta\sigma$ estimates for the Darfield earthquake and its aftershocks) the most optimally oriented fault in the network (HAF) does not rupture, and ruptures initiating on the HAF and SKF do not propagate beyond these sources, and (iii) for CSC_{max}^{crit} thresholds variably assigned to either 1 or 5 MPa depending on slip tendency, all hypocentral sources trigger rupture

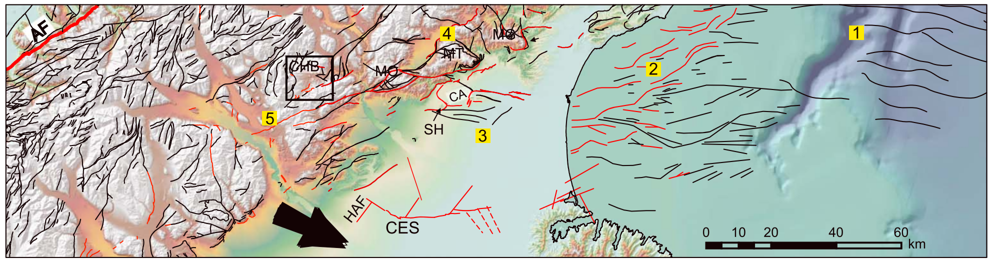

Figure 9. Map showing transect across Canterbury from offshore E-W inactive normal faults (1), through progressive fault system development (2 offshore; 3 onshore) towards a mature state (4 and 5 show the Porters Pass-Amberley Fault system). CA = Cust Anticline; CES = Canterbury Earthquake Sequence area; CHB = Castle Hill Basin; HAF = Hororata Anticline Fault; MO = Mount Oxford; MT = Mount Thomas; MG = Mount Grey; SH = Starvation Hill.

cascades across the entire network, except for ruptures initiating on the HAF and CCF_N (Figure 8) where CSC_{max} on adjacent receiver faults is limited to ~2.2 MPa in isolated pixels at fault intersections with misoriented faults. The slip tendency-integrated CSC_{max} model successfully replicates the Darfield earthquake and is our preferred model for rupture scenarios initiating on distinct hypocentral faults. Our conclusions are consistent with previously proposed hypotheses that the nucleation and propagation of large earthquakes on multifault networks is largely controlled by the geometric compatibility of adjacent fault junctions resulting from distinctly oriented intersecting faults (Gabrielov et al., 1996). CSC modeling suggests that cascading, multifault M_w 7.1 earthquakes analogous to the 2010 Darfield earthquake are more likely to occur (71% occurrence) than spatiotemporally distinct, smaller magnitude earthquakes that terminate within the hypocentral source fault (29% occurrence), if all the recognized source faults are equally capable of hosting the hypocentral rupture. This highlights the importance of understanding system behavior when evaluating the seismic hazard posed by individual faults.

Structurally analogous fault systems are present throughout the orogenic foreland of New Zealand's Southern Alps. Examples include the thrust fault-linked, E-W Oxford, Ashley-Loburn, Boby's Creek, and Birch Faults of North Canterbury (Barrell & Begg, 2013; Nicol, 1993; Nicol et al., 1994; Sisson et al., 2001) and probably several buried equivalents (Ghisetti & Sibson, 2012). Numerous global examples of analogous fault systems have also been documented; these include many European fault systems such as the Rhine Graben (Giamboni et al., 2004) and the source fault of France's largest instrumentally recorded 1909 Lambesc (Provence) earthquake that links into adjoining strike-slip faults that did not rupture (Chardon & Bellier, 2003), and active fault systems in California (Hauksson et al., 2002), Anatolia (Barka & Reilinger, 1997), North Africa (King & Yielding, 1984), and Iran (Berberian et al., 1999) that exhibit similar geometric properties. The rupture behavior, and particularly the potential for cascading ruptures of such fault systems, could be evaluated using similar methods to those described herein.

Our fault slip tendency analysis and CSC modeling indicate that the NE-SW orientated HAF fault may host isolated ruptures with faster slip rates and shorter recurrence intervals than complete multifault rupture scenarios. Thrust faults such as HAF are favorably aligned to the regional stress field to accommodate shortening via uplift (Figure 9). This provides a structurally based hypothesis for progressive orogenic uplift of the Southern Alps out of a system dominated by inherited large, structurally mature, optimally E-W oriented strike-slip faults (Barnes et al., 2016; Figure 9). Geometric constraints imposed on mature strike-slip faults by neighboring misoriented faults could allow optimally oriented thrusts to grow via tip propagation and segment capture while their strike-slip counterparts wane in activity or are kinematically captured within the developing orogen. This spatiotemporal progression can be seen in the transition from the strong inherited E-W fabric in the fault systems of the Canterbury Plains; through the more evolved but similar systems that bound major range-front peaks such as Mt Oxford, Thomas and Grey; to the relatively long, continuous faults that mark the inner ranges (Figure 9). Relict systems of diversely oriented faults may be preserved in intramontane basins such as Castle Hill Basin (Figure 9), where they reveal the underlying complexity of the orogen (Bradshaw, 1975). Hypotheses regarding the importance of geometric constraints on the growth of optimally oriented faults could be tested by comparing rupture chronologies and slip rates for multiple faults within fault networks and comparing these to fault geometric characteristics including their position within multifault networks.

10.1029/2019JB017508

We note that the optimal or misorientation of a hypocentral fault to regional stresses may not be the primary control on its ability to initiate a multifault rupture cascade. The geometric position of the source fault relative to its nearest neighbors within the network is demonstrably more important from the perspective of near-field static stress transfer. We do not know whether earthquakes occur more frequently (and/or with faster slip rates) on optimally oriented faults that are peripheral (less connected) to the network (e.g., HAF) relative to earthquakes on optimally oriented faults that are structurally pinned by junctions with misoriented faults (e.g., GF_C) that might regulate their behavior (Fletcher et al., 2016b). If this is the case, then additional contributions of smaller M_w events confined to isolated but optimally oriented faults could influence earthquake frequency-magnitude distributions over the time scales represented by successive ruptures on confined, optimally oriented faults and/or multifault rupture cascades.

5.3. Influence of Multifault Earthquake Cascades on Earthquake Frequency-Magnitude Distributions and Seismic Hazard

Earthquake frequency-magnitude, frequency-source size, and fault population frequency-length distributions exhibit scale invariance that can be statistically represented with power laws (Main, 1996; Turcotte, 1997) such as the G-R relationship (Gutenberg & Richter, 1944). At confined spatiotemporal scales (e.g., a mainshock-aftershock sequence in a specified region) the population of earthquakes with increasing M_L (e.g., approaching the mainshock M_L) commonly deviates from predicted populations using G-R scaling parameters established at lower M_L. The overpopulation of large M_L events relative to G-R scaling predictions has been interpreted as evidence for characteristic earthquake behavior for decades (Schwartz & Coppersmith, 1984).

Here we show that a recent hypothesis for characteristic earthquake behavior in the Darfield earthquake near-source region (Stirling & Zúñiga, 2017) cannot be statistically validated against a G-R scaling hypothesis because (i) the truncation of the CES seismicity catalogue in 2016 is unjustified; ongoing annual seismicity rates are still elevated compared to pre-mainshock rates (Quigley et al., 2016) (ii) the pre-Darfield annual seismicity rates at depths of ≤12 km could be significantly higher than seismicity rates derived by extrapolating the CES seismicity over a 20,000-year period, therefore the assumption that the CES seismicity catalogue represents a complete seismic catalogue between mainshock recurrence is not defensible, and (iii) the paleoseismologically defined recurrence interval of 20–30 kyr is developed for only one fault (GF_C) among the complex multifault network, and it is possible that other faults in this network may host large earthquakes more frequently than the GF. Furthermore, the large intrafault vertical and horizontal fault slip gradients and shallow depths of slip maxima (e.g., 1- to 5-km depth on the GF_C) observed in geodetic source models (Beavan et al., 2012) suggest additional earthquakes may be required to smooth finite slip distributions and avoid space problems. The few near-source aftershocks ($M_w \leq 5$ to 5.5) are unlikely to have generated cumulative coseismic displacements large enough to balance the surplus of shallow slip recorded during mainshock rupture. When considering the vast array of epistemic and statistical uncertainties (some of which are represented by Poissonian and Gaussian distributions in Figure 7) neither characteristic distribution nor G-R distribution can be unequivocally demonstrated to provide the best model for the Darfield earthquake source fault region.

Deaggregation of the Darfield earthquake into distinct M_L estimates based on fault size and slip (Beavan et al., 2012) and comparison with the seismologically observed frequency-magnitude distribution provides important insights into the role of system supercriticality in multifault earthquake rupture dynamics (Main, 1996; Scholz, 1990). The source deaggregated CES catalogue (Figure 7a) deviates significantly from the 95% Gaussian and Poissonian upper limits of the CES observed catalogue because the number of faults capable of independently generating $5 \leq M_L \leq 6.6$ earthquakes exceeds the number of observed earthquakes in this M_L range. The assembly of multiple $M_L \geq 6$ earthquakes to generate a M_L 7.1 event in the Darfield earthquake creates a sparsity of $5.5 \leq M_L \leq 6.6$ earthquakes relative to G-R scaling because these events occurred as part of the M_w 7.1 earthquake.

Earthquakes are a structural process (Sibson, 1989). Consistent with the hypothesis of Fletcher et al. (2016b) we posit that large earthquake recurrence on optimally oriented faults is controlled by fault system geometry. Strain is accumulated to the point of system supercriticality on optimally orientated faults, but cascading failure is controlled by faults with lower slip tendency (i.e., misorientated faults). Point criticality for

10.1029/2019JB017508

individual faults might be reached, but large ruptures do not occur because the growth of incipient ruptures is geometrically and kinematically dependent on the rupture of neighboring fault (Fletcher et al., 2016b). Whether the CCF represents a keystone fault that ultimately modulates system behavior (Fletcher et al., 2016b) or is simply a witnessed example of a suite of possible rupture scenarios is the subject of future investigation.

Because the CES seismicity catalogue reflects aftershock activity from the multifault earthquake (rather than spatiotemporally distinct ruptures on separate source faults), we do not know whether the aftershock sequence might have been more productive for incremental $5.5 \leq M_L \leq 6.6$ earthquakes (and thus more consistent with G-R scaling in this magnitude range for the deaggregated catalogue). $M_w{}^{max}$ in the deaggregated catalogue is not set by the largest fault source size ($M_w{}^{max} = 6.8$) but set by the largest observed earthquake in the seismicity data that ruptured all known sources ($M_w{}^{max} = 7.1 \pm 0.2$). We note that this estimate of $M_w{}^{max}$ is constrained only to rupture of the geodetically defined faults (Beavan et al., 2012); concurrent rupture of other unrecognized faults in both the near and far fields could result in a larger M_w earthquake (Hamling et al., 2017).

6. Conclusions

1. CSC modeling using rupture failure thresholds (CSC^{crit}) informed by empirically-derived stress drops and Mohr-Coulomb fault slip tendency analyses successfully replicates previously published rupture models of the Darfield earthquake. Progressive fault rupture occurred across multiple faults with different slip tendencies.
2. Application of the CSC approach with slip tendencies for different hypocentral source fault scenarios results in cascading multifault (M_w 7.1) ruptures across the fault system in five out of seven scenarios. Rupture propagation occurs irrespective of hypocentral source fault slip tendency. However, ruptures that initiate on peripheral faults may not propagate on to neighboring faults with low slip tendency; these earthquakes instead generate M_w 6.3 earthquakes that are restricted to the source fault. Earthquake magnitude distributions expected from the fault system relate to hypocentral source fault location and the geometric configuration of faults and their junctions within the network. This effect is likely to be important for earthquake dynamics on analogous fault systems in New Zealand and globally.
3. System behavior regulated by fault network geometries and slip tendencies influences the shape of the earthquake frequency-magnitude distribution, creates discrepancies between the source deaggregated magnitudes and observed magnitudes, and influences estimates of maximum magnitude ($M_w{}^{max}$). For cascading multifault ruptures, the frequency-magnitude distributions in the magnitude range of individual source contributions (e.g., M_w 6–6.8) may be lower than G-R scaling expectations because these sources commonly combine to generate larger magnitude earthquakes (e.g., M_w 7.1) that may (or may not) exceed recurrence based on G-R scaling. System $M_w{}^{max}$ relates to the largest magnitude that could arise from a combined multifault rupture; in many cases this might greatly exceed the $M_w{}^{max}$ emanating from any one fault in the system (Fletcher et al., 2016b). Conversely, relative to G-R scaling the source deaggregated catalogues may have increased populations of events in the magnitude range of individual source contributions. Lower $M_w{}^{max}$ estimates for deaggregated catalogues exist because the true $M_w{}^{max}$ of the system results from an amalgamated multifault earthquake rather than the $M_w{}^{max}$ arising from rupture of the largest fault.
4. The interpretation that an apparent increase in the frequency of large M_L events relative to G-R scaling predictions in the Darfield earthquake near-source region reflects characteristic behavior (Stirling & Zúñiga, 2017) is not statistically supported against the alternative G-R hypothesis if possible inputs from background seismicity and variations in b values are considered.
5. Observations from the Darfield earthquake are consistent with rupture nucleation on one of the most misoriented faults within the fault network that cascaded on to more optimally oriented faults. The hypocentral fault is strongly geometrically and kinematically connected to neighboring faults and thus occupies a key position within the fault network that may encourage or retard rupture propagation. The lack of well exposed cross cutting relationships do not allow us to know for certain if the hypocentral fault should be considered a "keystone fault," a fault whose misorientation controls the stability of the complex network and regulates slip on more optimally oriented neighboring faults until it ruptures (Fletcher et al., 2016b). However, the misoriented CCF was the first fault to rupture, and thus, it must

10.1029/2019JB017508

have been closer to failure than many other more optimally oriented faults in the network, a scenario that is counterintuitive without slip regulation by a keystone fault. Additionally, all other multifault rupture scenarios documented in this study require CSC^{crit} values that are relatively low compared to the large differences in slip tendency among the faults that ruptured. Therefore, network stability maintained by at least one misoriented keystone fault is the most likely mechanical explanation for both the observed and hypothetical multifault rupture scenarios discussed in this study. Optimally oriented faults (e.g., HAF) at the periphery of the network that intersect misoriented faults may rupture separately and thus have slip rates and earthquake chronologies distinct from the rest of the system.

Acknowledgments

The use of CSC modeling to study the Darfield earthquake was stimulated by discussions with Sandy Stacey. Frequency-scaling analysis benefited from discussions with Mark Stirling. We thank John Ristau and Anna Kaiser for provision of seismologic and stress drop data and subsequent discussions on these data. This paper greatly benefited from detailed and professional reviews by John Fletcher (CICESE) and constructive comments from an anonymous reviewer. All CSC data and results for all experiments, including tables, static images, and videos, are available at https://eartharxiv.org/v8t3n/ (DOI: 10.31223/osf.io/v8t3n).

References

Aki, K. (1965). Maximum likelihood estimate of b in the formula logN = a-bM and its confidence limits. *Bulletin of the Earthquake Research Institute*, *43*, 237–239.

Allmann, B. P., & Shearer, P. M. (2009). Global variations of stress drop for moderate to large earthquakes. *Journal of Geophysical Research*, *114*, B01310. https://doi.org/10.1029/2008JB005821

Allmendinger, R. W., Cardozo, N., & Fisher, D. M. (2012). *Structural Geology Algorithms: Vectors and Tensors*. Cambridge, UK: Cambridge University Press.

Angelier, J. (1989). From orientation to magnitudes in paleostress determinations using fault slip data. *Journal of Structural Geology*, *11*(1-2), 37–50.

Atzori, S., Tolomei, C., Antonioli, A., Merryman Boncori, J. P., Bannister, S., Trasatti, E., et al. (2012). The 2010-2011 Canterbury, New Zealand, seismic sequence: Multiple source analysis from InSAR data and modeling. *Journal of Geophysical Research*, *117*, B08305. https://doi.org/10.1029/2012JB009178

Bak, P., Tang, C., & Wiesenfeld, K. (1988). Self-organized criticality. *Physical Review A*, *38*(1), 364–374.

Bannister, S., & Gledhill, K. (2012). Evolution of the 2010–2012 Canterbury earthquake sequence. *New Zealand Journal of Geology and Geophysics*, *55*(3), 295–304. https://doi.org/10.1080/00288306.2012.680475

Barka, A., & Reilinger, R. (1997). Active tectonics of the Eastern Mediterranean region: Deduced from GPS, neotectonic and seismicity data. *Annali di Geofisica*, *40*(3), 587–610.

Barnes, P. M., Ghisetti, F. C., & Gorman, A. R. (2016). New insights into the tectonic inversion of North Canterbury and the regional structural context of the 2010–2011 Canterbury earthquake sequence, New Zealand, Geochemistry, Geophysics. *Geosystems*, *17*(2), 324–345. https://doi.org/10.1002/2015GC006069

Barrell, D., & Begg, J. (2013). General distribution and characteristics of active faults and folds in the Waimakariri District, North Canterbury, GNS Science Consultancy Report 2012/326, 61pp.

Beavan, J., Motagh, M., Fielding, E., Donnelly, N., & Collett, D. (2012). Fault slip models of the 2010-2011 Canterbury, New Zealand, earthquakes from geodetic data, and observations of post-seismic ground deformation. *New Zealand Journal of Geology and Geophysics*, *55*(3), 207–221. https://doi.org/10.1080/00288306.2012.697472

Ben-Zion, Y., & Sammis, C. G. (2003). Characterization of fault zones. *Pure and Applied Geophysics*, *160*(3-4), 677–715.

Berberian, M., Jackson, J. A., Qorashi, M., Khatib, M. M., Priestley, K., Talebian, M., & Ghafuri-Ashtiani, M. (1999). The 1997 May 10 Zirkuh (Qa'enat) earthquake (M(w) 7.2): Faulting along the Sistan suture zone of eastern Iran. *Geophysical Journal International*, *136*(3), 671–694. https://doi.org/10.1046/j.1365-246X.1999.00762.x

Beroza, G. C., & Ellsworth, W. L. (1996). Properties of the seismic nucleation phase. *Tectonophysics*, *261*(1-3), 209–227.

Bhat, H. S., Dmowska, R., Rice, J. R., & Kame, N. (2004). Dynamic slip transfer from the Denali to Totschunda Faults, Alaska: Testing theory for fault branching. *Bulletin of the Seismological Society of America*, *94*(6B), S202–S213. https://doi.org/10.1785/0120040601

Bowman, J. (1992). The 1988 Tennant Creek, northern territory, earthquakes: A synthesis. *Australian Journal of Earth Sciences*, *39*(5), 651–669.

Bradshaw, J. D. (1975). The folds at Castle Hill (Canterbury) and their bearing on the Kaikouran deformation style in the Canterbury Basin. *Journal of the Royal Society of New Zealand*, *5*(2), 209–217.

Chardon, D., & Bellier, O. (2003). Geological boundary conditions of the 1909 Lambesc (Provence, France) earthquake: Structure and evolution of the Trévaresse ridge anticline. *Bulletin de la Societe Geologique de France*, *174*(5), 497–510.

Cocco, M., & Rice, J. R. (2002). Pore pressure and poroelasticity effects in Coulomb stress analysis of earthquake interactions. *Journal of Geophysical Research*, *107*(B2), 2030. https://doi.org/10.1029/2000JB000138

Dieterich, J. H. (1992). Earthquake nucleation on faults with rate-and state-dependent strength. *Tectonophysics*, *211*(1-4), 115–134.

Douilly, R., Aochi, H., Calais, E., & Freed, A. M. (2015). Three-dimensional dynamic rupture simulations across interacting faults: The Mw 7.0, 2010, Haiti earthquake. *Journal of Geophysical Research: Solid Earth*, *120*, 1108–1128. https://doi.org/10.1002/2014JB011595

Eberhart-Phillips, D., Haeussler, P. J., Freymueller, J. T., Frankel, A. D., Rubin, C. M., Craw, P., et al. (2003). The 2002 Denali fault earthquake, Alaska: A large magnitude, slip-partitioned event. *Science*, *300*(5622), 1113–1118.

Elliott, J. R., Nissen, E. K., England, P. C., Jackson, J. A., Lamb, S., Li, Z., et al. (2012). Slip in the 2010 and 2011 Canterbury earthquakes, New Zealand. *Journal of Geophysical Research*, *117*, B03401. https://doi.org/10.1029/2011JB008868

Ellis, S., Williams, C., Ristau, J., Reyners, M., Eberhart-Phillips, D., & Wallace, L. M. (2016). Calculating regional stresses for northern Canterbury: The effect of the 2010 Darfield earthquake. *New Zealand Journal of Geology and Geophysics*, *59*(1), 202–212. https://doi.org/10.1080/00288306.2015.1123740

Field, E. H., Arrowsmith, R. J., Biasi, G. P., Bird, P., Dawson, T. E., Felzer, K. R., et al. (2014). Uniform California Earthquake Rupture Forecast, version 3 (UCERF3) -The time-independent model. *Bulletin of the Seismological Society of America*, *104*(3), 1122–1180. https://doi.org/10.1785/0120130164

Fletcher, J., M. Oskin, and O. Teran (2016a), The mechanics of multifault ruptures and the keystone fault hypothesis, Paper presented at AGU Fall Meeting Abstracts.

Fletcher, J. M., Oskin, M. E., & Teran, O. J. (2016b). The role of a keystone fault in triggering the complex El Mayor-Cucapah earthquake rupture. *Nature Geoscience*, *9*(4), 303–307. https://doi.org/10.1038/ngeo2660

Freed, A. M. (2005). Earthquake triggering by static, dynamic, and postseismic stress transfer. *Annual Review of Earth and Planetary Sciences*, *33*(1), 335–367. https://doi.org/10.1146/annurev.earth.33.092203.122505

Fry, B., & Gerstenberger, M. C. (2011). Large apparent stresses from the Canterbury earthquakes of 2010 and 2011. *Seismological Research Letters*, *82*(6), 833–838. https://doi.org/10.1785/gssrl.82.6.833

Gabrielov, A., Keilis-Borok, V., & Jackson, D. D. (1996). Geometric incompatibility in a fault system. *Proceedings of the National Academy of Sciences of the United States of America*, *93*(9), 3838–3842.

Gerstenberger, M., McVerry, G., Rhoades, D., & Stirling, M. (2014). Seismic hazard modeling for the recovery of Christchurch. *Earthquake Spectra*, *30*(1), 17–29. https://doi.org/10.1193/021913EQS037M

Ghisetti, F. C., & Sibson, R. H. (2012). Compressional reactivation of E-W inherited normal faults in the area of the 2010-2011 Canterbury earthquake sequence. *New Zealand Journal of Geology and Geophysics*, *55*(3), 177–184.

Giamboni, M., Ustaszewski, K., Schmid, S. M., Schumacher, M. E., & Wetzel, A. (2004). Plio-Pleistocene transpressional reactivation of Paleozoic and Paleogene structures in the Rhine-Bresse transform zone (northern Switzerland and eastern France). *International Journal of Earth Sciences*, *93*(2), 207–223. https://doi.org/10.1007/s00531-003-0375-2

Gledhill, K., Ristau, J., Reyners, M., Fry, B., Holden, C., & GeoNet-Team (2010). The Darfield (Canterbury) earthquake of September 2010: Preliminary seismological report. *Bulletin of the New Zealand Society for Earthquake Engineering*, *43*(4), 215–221.

Gomberg, J., Bodin, P., & Reasenberg, P. A. (2003). Observing earthquakes triggered in the near field by dynamic deformations. *Bulletin of the Seismological Society of America*, *93*(1), 118–138.

Gutenberg, B., & Richter, C. F. (1944). Frequency of earthquakes in California. *Bulletin of the Seismological Society of America*, *34*, 185–188.

Hainzl, S., Enescu, B., Cocco, M., Woessner, J., Catalli, F., Wang, R., & Roth, F. (2009). Aftershock modeling based on uncertain stress calculations. *Journal of Geophysical Research*, *114*, B05309. https://doi.org/10.1029/2008JB006011

Hamling, I. J., Hreinsdóttir, S., Clark, K., Elliott, J., Liang, C., Fielding, E., et al. (2017). Complex multifault rupture during the 2016 Mw 7.8 Kaikōura earthquake, New Zealand. *Science*, *356*(6334), eaam7194. https://doi.org/10.1126/science.aam7194

Hanks, T. C., & Thatcher, W. (1972). A graphical representation of seismic source parameters. *Journal of Geophysical Research*, *77*(23), 4393–4405. https://doi.org/10.1029/JB077i023p04393

Harris, R. A. (1998). Introduction to special section: Stress triggers, stress shadows, and implications for seismic hazard. *Journal of Geophysical Research*, *103*, 24,347–24,358. https://doi.org/10.1029/98JB01576

Harris, R. A. (2000). Earthquake stress triggers, stress shadows, and seismic hazard. *Current Science*, *103*, 1215–1225.

Harris, R. A., & Day, S. M. (1993). Dynamics of fault interaction: Parallel strike-slip faults. *Journal of Geophysical Research*, *98*(B3), 4461–4472. https://doi.org/10.1029/92JB02272

Harris, R. A., & Day, S. M. (1999). Dynamic 3D simulations of earthquakes on en echelon faults. *Geophysical Research Letters*, *26*(14), 2089–2092. https://doi.org/10.1029/1999GL900377

Hauksson, E., Jones, L. M., & Hutton, K. (2002). The 1999 Mw 7.1 Hector Mine, California, earthquake sequence: Complex conjugate strike-slip faulting. *Bulletin of the Seismological Society of America*, *92*(4), 1154–1170. https://doi.org/10.1785/0120000920

Hayes, G. P. (2010). The M7.0 South Island, New Zealand Earthquake of 3 September, 2010. United States Geological Survey Summary Poster, edited, USGS.

Hayes, G. P., Briggs, R. W., Sladen, A., Fielding, E. J., Prentice, C., Hudnut, K., et al. (2010). Complex rupture during the 12 January 2010 Haiti earthquake. *Nature Geoscience*, *3*(11), 800–805. https://doi.org/10.1038/ngeo977

Herman, M. W., Herrmann, R. B., Benz, H. M., & Furlong, K. P. (2014). Using regional moment tensors to constrain the kinematics and stress evolution of the 2010–2013 Canterbury earthquake sequence, South Island, New Zealand. *Tectonophysics*, *633*, 1–15. https://doi.org/10.1016/j.tecto.2014.06.019

Holden, C., Beavan, J., Fry, B., Reyners, M., Ristau, J., van Dissen, R., et al. (2011). Preliminary source model of the M_W 7.1 Darfield earthquake from geological, geodetic and seismic data, Paper presented at Ninth Pacific Conference on Earthquake Engineering, Building an Earthquake-Resilient Society, Paper 164, 7 p., New Zealand Society for Earthquake Engineering, Auckland, New Zealand.

Hornblow, S., Quigley, M., Nicol, A., Van Dissen, R., & Wang, N. (2014). Paleoseismology of the 2010 Mw 7.1 Darfield (Canterbury) earthquake source, Greendale Fault, New Zealand. *Tectonophysics*, *637*, 178–190. https://doi.org/10.1016/j.tecto.2014.10.004

Howell, B. F. (1985). On the effect of too small a data base on earthquake frequency diagrams. *Bulletin of the Seismological Society of America*, *75*(4), 1205–1207.

Ishimoto, M., & Lida, K. (1939). Observations of earthquakes registered with the microseismograph constructed recently. *Bulletin of the Earthquake Research Institute*, *17*, 443–478.

Ito, Y., Ikari, M. J., Ujiie, K., & Kopf, A. (2017). Coseismic slip propagation on the Tohoku plate boundary fault facilitated by slip-dependent weakening during slow fault slip. *Geophysical Research Letters*, *44*, 8749–8756. https://doi.org/10.1002/2017GL074307

Kagan, Y. Y. (1993). Statistics of characteristic earthquakes. *Bulletin of the Seismological Society of America*, *83*(1), 7–24.

Kagan, Y. Y. (1996). VAN earthquake predictions—An attempt at statistical evaluation. *Geophysical Research Letters*, *23*(11), 1315–1318. https://doi.org/10.1029/95GL03417

Kagan, Y. Y., Jackson, D. D., & Geller, R. J. (2012). Characteristic earthquake model, 1884-2011, R.I.P. *Seismological Research Letters*, *83*(6), 951–953. https://doi.org/10.1785/0220120107

Kame, N., & Yamashita, T. (2003). Dynamic branching, arresting of rupture and the seismic wave radiation in self-chosen crack path modelling. *Geophysical Journal International*, *155*(3), 1042–1050. https://doi.org/10.1111/j.1365-246X.2003.02113.x

Kijko, A. (2004). Estimation of the maximum earthquake magnitude, m max. *Pure and Applied Geophysics*, *161*(8), 1655–1681.

King, G., Stein, R. S., & Lin, J. (1994). Static stress changes and the triggering of earthquakes. *Bulletin of the Seismological Society of America*, *84*(3), 935–953.

King, G., & Yielding, G. (1984). The evolution of a thrust fault system: Processes of rupture initiation, propagation and termination in the 1980 El Asnam (Algeria) earthquake. *Geophysical Journal International*, *77*(3), 915–933. https://doi.org/10.1111/j.1365-246X.1984.tb02229.x

Klinger, Y. (2010). Relation between continental strike-slip earthquake segmentation and thickness of the crust. *Journal of Geophysical Research*, *115*, B07306. https://doi.org/10.1029/2009JB006550

Lawton, D. C., Bertram, M. B., Hall, K. W., Bertram, K. L., & Pettinga, J. (2011). Post-earthquake seismic reflection survey, Christchurch, New Zealand *Rep.*, CREWES Research Report.

Li, Y. G., de Pascale, G. P., Quigley, M. C., & Gravley, D. M. (2014). Fault damage zones of the M7.1 Darfield and M6.3 Christchurch earthquakes characterized by fault-zone trapped waves. *Tectonophysics*, *618*, 79–101. https://doi.org/10.1016/j.tecto.2014.01.029

Litchfield, N. J., van Dissen, R., Sutherland, R., Barnes, P. M., Cox, S. C., Norris, R., et al. (2014). A model of active faulting in New Zealand. *New Zealand Journal of Geology and Geophysics*, *57*(1), 32–56. https://doi.org/10.1080/00288306.2013.854256

Lu, S. (2017). Long-term b value variations of shallow earthquakes in New Zealand: A HMM-based analysis. *Pure and Applied Geophysics*, *174*(4), 1629–1641. https://doi.org/10.1007/s00024-017-1482-5

Madariaga, R. (1976). Dynamics of an expanding circular fault. *Bulletin of the Seismological Society of America*, *66*(3), 639–666.

Mai, P. M., Spudich, P., & Boatwright, J. (2005). Hypocenter locations in finite-source rupture models. *Bulletin of the Seismological Society of America*, *95*(3), 965–980. https://doi.org/10.1785/0120040111

Main, I. (1996). Statistical physics, seismogenesis, and seismic hazard. *Reviews of Geophysics*, *34*(4), 433–462. https://doi.org/10.1029/96RG02808

Marrett, R. A., & Allmendinger, R. W. (1990). Kinematic analysis of fault-slip data. *Journal of Structural Geology*, *12*, 973–986.

McGuire, J. J., Zhao, L., & Jordan, T. H. (2002). Predominance of unilateral rupture for a global catalog of large earthquakes. *Bulletin of the Seismological Society of America*, *92*(8), 3309–3317. https://doi.org/10.1785/0120010293

McNamara, D. D., Faulkner, D., & McCarney, E. (2014). Rock properties of greywacke basement hosting geothermal reservoirs, New Zealand: Preliminary results, Paper presented at Thirty-Ninth Workshop on Geothermal Reservoir Engineering, Stanford University, Stanford, California.

Naylor, M., Greenhough, J., McCloskey, J., Bell, A. F., & Main, I. G. (2009). Statistical evaluation of characteristic earthquakes in the frequency-magnitude distributions of Sumatra and other subduction zone regions. *Geophysical Research Letters*, *36*, L20303. https://doi.org/10.1029/2009GL040460

Nicol, A. (1993). Haumurian (c.66–80 Ma) half-graben development and deformation, mid Waipara, north Canterbury, New Zealand. *New Zealand Journal of Geology and Geophysics*, *36*(1), 127–130.

Nicol, A., Alloway, B. V., & Tonkin, P. L. (1994). Rates of deformation, uplift and landscape development associated with active folding in the Waipara area of North Canterbury, New Zealand. *Tectonics*, *13*(6), 1327–1344. https://doi.org/10.1029/94TC01502

Nieto-Obregón, J. (1989). Tectonic synthesis and seismic risk along the Rio Grande de Santiago fault, in Jalisco, Mexico. *International Journal of Mining and Geological Engineering*, *7*(1), 37–51.

Oglesby, D. D., Mai, P. M., Atakan, K., & Pucci, S. (2008). Dynamic models of earthquakes on the North Anatolian fault zone under the Sea of Marmara: Effect of hypocenter location. *Geophysical Research Letters*, *35*, L18302. https://doi.org/10.1029/2008GL035037

Okada, Y. (1992). Internal deformation due to shear and tensile faults in a half-space. *Bulletin of the Seismological Society of America*, *82*(2), 1018–1040.

Olami, Z., Feder, H. J. S., & Christensen, K. (1992). Self-organized criticality in a continuous, nonconservative cellular automaton modeling earthquakes. *Physical Review Letters*, *68*(8), 1244–1247.

Oth, A., & Kaiser, A. (2014). Stress release and source scaling of the 2010–2011 Canterbury, New Zealand earthquake sequence from spectral inversion of ground motion data. *Pure and Applied Geophysics*, *171*(10), 2767–2782. https://doi.org/10.1007/s00024-013-0751-1

Pacheco, J. F., Scholz, C. H., & Sykes, L. R. (1992). Changes in frequency–size relationship from small to large earthquakes. *Nature*, *355*(6355), 71.

Page, M., & Felzer, K. (2015). Southern San Andreas fault seismicity is consistent with the Gutenberg–Richter magnitude–frequency distribution. *Bulletin of the Seismological Society of America*, *105*(4), 2070–2080. https://doi.org/10.1785/0120140340

Page, M. T., Alderson, D., & Doyle, J. (2011). The magnitude distribution of earthquakes near Southern California faults. *Journal of Geophysical Research*, *116*, B12309. https://doi.org/10.1029/2010JB007933

Parsons, T., Field, E. H., Page, M. T., & Milner, K. (2012). Possible earthquake rupture connections on mapped California faults ranked by calculated Coulomb linking stresses. *Bulletin of the Seismological Society of America*, *102*(6), 2667–2676. https://doi.org/10.1785/0120110349

Quigley, M., Jiménez, A., Duffy, B., & King, T. R. (2018). An investigation of multi-fault rupture scenarios using a variety of Coulomb stress modelling criteria: Methods paper and full results, EarthArXiv, doi: 10.31223/osf.io/v8t3n.

Quigley, M. C., & Forte, A. M. (2017). Science website traffic in earthquakes. *Seismological Research Letters*, *88*(3), 867–874. https://doi.org/10.1785/0220160172

Quigley, M. C., Hughes, M. W., Bradley, B. A., Ballegooy, S. V., Reid, C., Morgenroth, J., et al. (2016). The 2010–2012 Canterbury earthquake sequence: Environmental effects, seismic triggering thresholds and geologic legacy. *Tectonophysics*, *672-673*, 228–274. https://doi.org/10.1016/j.tecto.2016.01.044

Quigley, M. C., van Dissen, R., Litchfield, N., Villamor, P., Duffy, B., Barrell, D., et al. (2012). Surface rupture during the 2010 M_W 7.1 Darfield (Canterbury) earthquake: Implications for fault rupture dynamics and seismic-hazard analysis. *Geology*, *40*(1), 55–58. https://doi.org/10.1130/G32528.1

Rundle, J. B. (1989). Derivation of the complete Gutenberg-Richter magnitude-frequency relation using the principle of scale invariance. *Journal of Geophysical Research*, *94*(B9), 12,337–12,342. https://doi.org/10.1029/JB094iB09p12337

Sandri, L., & Marzocchi, W. (2007). A technical note on the bias in the estimation of the b-value and its uncertainty through the least squares technique. *Annals of Geophysics*, *50*(3), 329–339.

Scherbaum, F., & Kuehn, N. M. (2011). Logic tree branch weights and probabilities: Summing up to one is not enough. *Earthquake Spectra*, *27*(4), 1237–1251. https://doi.org/10.1193/1.3652744

Scholz, C. H. (1990). Earthquakes as chaos. *Nature*, *348*(6298), 197–198.

Scholz, C. H. (1997). Size distributions for large and small earthquakes. *Bulletin of the Seismological Society of America*, *87*(4), 1074–1077.

Scholz, C. H. (2002). *The Mechanics of Earthquakes and Faulting* (p. 473). Cambridge, UK: Cambridge University Press.

Scholz, C. H. (2010). Large earthquake triggering, clustering, and the synchronization of faults. *Bulletin of the Seismological Society of America*, *100*(3), 901–909.

Schwartz, D. P., & Coppersmith, K. J. (1984). Fault behavior and characteristic earthquakes: Examples from the Wasatch and San Andreas Fault Zones. *Journal of Geophysical Research*, *89*(B7), 5681–5698. https://doi.org/10.1029/JB089iB07p05681

Shaw, B. E. (2009). Constant stress drop from small to great earthquakes in magnitude-area scaling. *Bulletin of the Seismological Society of America*, *99*(2A), 871–875.

Shcherbakov, R., Nguyen, M., & Quigley, M. (2012). Statistical analysis of the 2010 M_W 7.1 Darfield Earthquake aftershock sequence. *New Zealand Journal of Geology and Geophysics*, *55*(3), 305–311. https://doi.org/10.1080/00288306.2012.676556

Sibson, R. H. (1989). Earthquake faulting as a structural process. *Journal of Structural Geology*, *11*(1/2), 1–14.

Sibson, R. H., Ghisetti, F. C., & Crookbain, R. A. (2012). *Andersonian wrench faulting in a regional stress field during the 2010–2011 Canterbury, New Zealand, earthquake sequence*. *Geological Society, London, Special Publications* (Vol. 367, pp. 7–18).

Sibson, R. H., Ghisetti, F. C., & Ristau, J. (2011). Stress control of an evolving strike-slip fault system during the 2010–2011 Canterbury, New Zealand, earthquake sequence. *Seismological Research Letters*, *82*(6), 824–832.

Sisson, R., Campbell, J., Pettinga, J., & Milner, D. (2001). Paleoseismicity of the Ashley and Loburn Faults, North Canterbury, New Zealand, Earthquake Commission Research Foundation report 97/237.

Spada, M., Tormann, T., Wiemer, S., & Enescu, B. (2013). Generic dependence of the frequency-size distribution of earthquakes on depth and its relation to the strength profile of the crust. *Geophysical Research Letters*, *40*, 709–714. https://doi.org/10.1029/2012GL054198

Steacy, S., Nalbant, S. S., McCloskey, J., Nostro, C., Scotti, O., & Baumont, D. (2005). Onto what planes should Coulomb stress perturbations be resolved? *Journal of Geophysical Research*, *110*, B05S15. https://doi.org/10.1029/2004JB003356

Stein, R. S. (1999). The role of stress transfer in earthquake occurrence. *Nature*, *402*(6762), 605–609.

Stein, R. S., Barka, A. A., & Dieterich, J. H. (1997). Progressive failure on the North Anatolian fault since 1939 by earthquake stress triggering. *Geophysical Journal International*, *128*(3), 594–604.

Stein, R. S., King, G. C., & Lin, J. (1992). Change in failure stress on the southern San Andreas fault system caused by the 1992 magnitude= 7.4 Landers earthquake. *Science*, *258*(5086), 1328–1332.

Stewart, S. (2007). Rock mass strength and deformability of unweathered closely jointed New Zealand greywacke, PhD thesis, University of Canterbury, Christchurch, New Zealand.

Stirling, M. W., & Zúñiga, F. R. (2017). Shape of the magnitude-frequency distribution for the Canterbury earthquake sequence from integration of seismological and geological data. *Bulletin of the Seismological Society of America*, *107*(1), 495–500. https://doi.org/10.1785/0120160246

Stock, C., & Smith, E. G. (2000). Evidence for different scaling of earthquake source parameters for large earthquakes depending on faulting mechanism. *Geophysical Journal International*, *143*(1), 157–162.

Stramondo, S., Kyriakopoulos, C., Bignami, C., Chini, M., Melini, D., Moro, M., et al. (2011). Did the September 2010 (Darfield) earthquake trigger the February 2011 (Christchurch) event? *Scientific Reports*, *1*. https://doi.org/10.1038/srep00098

Syracuse, E. M., Thurber, C. H., Rawles, C. J., Savage, M. K., & Bannister, S. (2013). High-resolution relocation of aftershocks of the M_w 7.1 Darfield, New Zealand, earthquake and implications for fault activity. *Journal of Geophysical Research: Solid Earth*, *118*, 4184–4195. https://doi.org/10.1002/jgrb.50301

Templeton, E. L., Baudet, A., Bhat, H. S., Dmowska, R., Rice, J. R., Rosakis, A. J., & Rousseau, C. E. (2009). Finite element simulations of dynamic shear rupture experiments and dynamic path selection along kinked and branched faults. *Journal of Geophysical Research*, *114*, B08304. https://doi.org/10.1029/2008JB006174

Templeton, E. L., Bhat, H. S., Dmowska, R., & Rice, J. R. (2010). Dynamic rupture through a branched fault configuration at Yucca Mountain, and resulting ground motions. *Bulletin of the Seismological Society of America*, *100*(4), 1485–1497. https://doi.org/10.1785/0120090121

Triep, E. G., & Sykes, L. R. (1997). Frequency of occurrence of moderate to great earthquakes in intracontinental regions: Implications for changes in stress, earthquake prediction, and hazards assessments. *Journal of Geophysical Research*, *102*(B5), 9923–9948. https://doi.org/10.1029/96JB03900

Turcotte, D. L. (1997). *Fractals and Chaos in Geology and Geophysics* (pp. 148–149). Cambridge, UK: Cambridge University Press.

Utsu, T. (1966). A statistical significance test of the difference in b-value between two earthquake groups. *Journal of Physics of the Earth*, *14*(2), 37–40. https://doi.org/10.4294/jpe1952.14.37

Walters, R. J., Gregory, L. C., Wedmore, L., Craig, T. J., McCaffrey, K., Wilkinson, M., et al. (2018). Dual control of fault intersections on stop-start rupture in the 2016 central Italy seismic sequence. *Earth and Planetary Science Letters*, *500*, 1–14.

Wesnousky, S. G. (1994). The Gutenberg-Richter or characteristic earthquake distribution, which is it? *Bulletin of the Seismological Society of America*, *84*(6), 1940–1959.

Woessner, J., Jonsson, S., Sudhaus, H., & Baumann, C. (2012). Reliability of Coulomb stress changes inferred from correlated uncertainties of finite-fault source models. *Journal of Geophysical Research*, *117*, B07303. https://doi.org/10.1029/2011JB009121

Woessner, J., & Wiemer, S. (2005). Assessing the quality of earthquake catalogues: Estimating the magnitude of completeness and its uncertainty. *Bulletin of the Seismological Society of America*, *95*(2), 684–698. https://doi.org/10.1785/0120040007

Zhan, Z., Wei, S., Ni, S., & Helmberger, D. (2011). Earthquake centroid locations using calibration from ambient seismic noise. *Bulletin of the Seismological Society of America*, *101*(3), 1438–1445.

Zoback, M. D., & Townend, J. (2001). Implications of hydrostatic pore pressures and high crustal strength for the deformation of intraplate lithosphere. *Tectonophysics*, *336*(1), 19–30. https://doi.org/10.1016/S0040-1951(01)00091-9

Zúñiga, F. R., Reyners, M., & Villamor, P. (2005). Temporal variations of the earthquake data in the catalogue of seismicity of New Zealand. *Bulletin of the New Zealand Society for Earthquake Engineering*, *38*(2), 87–105.